Department of Applied Mechanics

Damage Modelling Procedure and Fastener Positioning Optimization of Adhesively Reinforced Frictional Interfaces

Ahti Oinonen

Aalto University

DOCTORAL DISSERTATIONS

Ahti Oinonen

Damage Modelling Procedure and Fastener Positioning Optimization of Adhesively Reinforced Frictional Interfaces

Aalto University

Aalto University publication series
DOCTORAL DISSERTATIONS 91/2011

Damage Modelling Procedure and Fastener Positioning Optimization of Adhesively Reinforced Frictional Interfaces

Ahti Oinonen

Doctoral dissertation for the degree of Doctor of Science in Technology to be presented with due permission of the School of Engineering for public examination and debate in Auditorium K1/215 at the Aalto University School of Engineering (Espoo, Finland) on the 28th of November 2011 at 12 noon.

Aalto University
School of Engineering
Department of Applied Mechanics
Mechanics of Materials

Supervisor
Professor Gary Marquis

Instructor
Professor Gary Marquis

Preliminary examiners
Professor Alessandro Pirondi
University of Parma
Italy

Professor Zhiliang Zhang
Norwegian University of Science and Technology
Norway

Opponents
Professor Michael Vormwald
Technische Universität Darmstadt
Germany

Aalto University publication series
DOCTORAL DISSERTATIONS 91/2011

ISBN 978-952-60-4305-0 (pdf)
ISBN 978-952-60-4304-3 (printed)
ISSN-L 1799-4934
ISSN 1799-4942 (pdf)
ISSN 1799-4934 (printed)

Aalto Print
Helsinki 2011

Finland

The dissertation can be read at http://lib.tkk.fi/Diss/

Aalto University

Abstract

Aalto University, P.O. Box 11000, FI-00076 Aalto www.aalto.fi

Author
Ahti Oinonen

Name of the doctoral dissertation
Damage Modelling Procedure and Fastener Positioning Optimization of Adhesively Reinforced Frictional Interfaces

Publisher School of Engineering

Unit Department of Applied Mechanics

Series Aalto University publication series DOCTORAL DISSERTATIONS 91/2011

Field of research Mechanics of Materials

Manuscript submitted 13 June 2011 **Manuscript revised** 15 September 2011

Date of the defence 28 November 2011 **Language** English

☒ **Monograph** ☐ **Article dissertation (summary + original articles)**

Abstract

This thesis is concerned with the development of the shear damage simulation procedure for combined mechanically clamped and adhesively reinforced frictional joint interfaces. The first step has been to experimentally measure the shear fracture behaviour of high strength steel interfaces using annular ring specimens subject to constant normal pre-stress. The experimental programme included variations of the pre-stress, surface roughness and epoxy curing temperature. Results showed that these factors significantly influence both the maximum attainable peak shear loads and the critical fracture energy release rate of the interfaces. For the selected structural adhesive, the strength contributions of the reinforcing adhesive and friction due to the pre-stress conformed well to the principle of superposition. Comparisons of adhesively reinforced and non-reinforced interfaces with identical surface conditions and pre-stress demonstrate a substantial contribution due to the epoxy reinforcement.

Test results are exploited for characterization of the non-local shear stress vs. displacement responses. A damage evolution model for the abraded interface is formulated for room temperature- and heat-cured adhesives. Model parameters are fitted using regression analysis. Decohesion finite elements involving the cohesive zone model are adapted to model progressive degradation of the reinforced interfaces. A non-local friction law is also implemented when modelling the surface interaction using finite element contact. Based on the principle of superposition, the fracture potential and steady frictional dissipation of the interface can, therefore, be independently characterized.

An applicability of the presented damage simulation process is shown by finite element analyses on the structural multi-fastener connections. Corresponding experiments on full-scale joints were performed. The measured peak shear loads show a good correlation with the computed results. To further strengthen multi-fastener connections, a geometric optimization procedure is formulated for equalizing fastener loads due to an applied eccentric load.

In summary, the objective of this thesis is to develop a damage simulation procedure to analyse decohesion initiation of adhesively reinforced frictional interfaces under quasi-static shear loading. Both the numerical modelling procedure and new material property data for a design of more optimal structures involving multi-fastener connections are presented.

Keywords Cohesive zone modelling, damage mechanics, geometric optimization, interface fracture

ISBN (printed) 978-952-60-4304-3 **ISBN (pdf)** 978-952-60-4305-0

ISSN-L 1799-4934 **ISSN (printed)** 1799-4934 **ISSN (pdf)** 1799-4942

Location of publisher Espoo **Location of printing** Helsinki **Year** 2011

Pages 107 **The dissertation can be read at** http://lib.tkk.fi/Diss/

Tekijä
Ahti Oinonen

Väitöskirjan nimi
Rakenneliimalla vahvistettujen kitkarajapintojen vauriomallinnusprosessi ja kiinnittimien sijoitteluoptimointi

Julkaisija Insinööritieteiden korkeakoulu

Yksikkö Sovelletun mekaniikan laitos

Sarja Aalto University publication series DOCTORAL DISSERTATIONS 91/2011

Tutkimusala Lujuusoppi

Käsikirjoituksen pvm 13.06.2011 **Korjatun käsikirjoituksen pvm** 15.09.2011

Väitöspäivä 28.11.2011 **Kieli** Englanti

☒ **Monografia** ☐ **Yhdistelmäväitöskirja (yhteenveto-osa + erillisartikkelit)**

Tiivistelmä

Tässä väitöskirjatyössä kehitetään etenevän leikkausvaurion mallinnusprosessi rakenneliimalla vahvistetuille kitkaliitosrajapinnoille. Aluksi suurlujuusteräsrajapintojen leikkausvauriokäyttäytyminen määritettiin perustutkimustasolla käyttäen normaalin suuntaisesti tasaisesti kuormitettuja kiekkokoekappaleita. Kokeelliseen tutkimusohjelmaan sisältyi erilaisten esikiristysarvojen, kontaktipinnankarheuden ja liiman kovettamislämpötilojen variaatioita. Tulosten perusteella nämä tekijät myötävaikuttavat maksimaalisen rajapinnan leikkauslujuuden ja krittisen murtumisenergiadissipaation saavuttamisessa. Esikiristyksen ja valitulla epoksiliimalla saavutetun lujuusvaikutusten havaittiin noudattavan superpositioperiaatetta. Rakenneliimalla vahvistettujen kitkarajapintojen lujuus havaittiin huomattavasti suuremmaksi verrattuna vastaaviin liimaamattomiin koekappaleisiin.

Saavutettuja koetuloksia hyödynnetään jännitys-siirtymävasteen yksityiskohtaisessa määrittämisessä. Parametrinen koheesiomalli muodostetaan karkealle rajapintatyypille sekä huoneenlämpötilassa kovetetulle että lämpökovetetulle epoksiliimalle. Lujuusopin elementtimenetelmässä käytetään koheesioelementtejä jatkuvan rajapintavaurion kuvaamiseksi. Lisäksi vaurioituvalle kontaktirajapinnalle mallinnetaan vaikuttamaan kitka. Vaurioituvan rajapinnan murtumisenergiapotentiaali ja ajasta riippumaton kitkadissipaatio voidaan siten karakterisoida toisistaan riippumattomina perustuen superpositioperiaatteeseen.

Esitetyn vaurion simulointiprosessin sovellettavuus osoitetaan analysoimalla monikiinnitinliitosten leikkauslujuutta lujuusopin elementtimenetelmään perustuen. Simulointimallia vastaavien täysmittakaavaisten koesauvojen lujuutta testattiin lisäksi laboratoriokokein. Mitatut maksimileikkauskuormat korreloivat hyvin vastaavien numeerisen laskennan tulosten kanssa. Lisäksi työssä formuloidaan epäkeskeisesti kuormitetulle liitokselle geometrinen optimointitehtävä, jota hyödyntämällä voidaan saavuttaa tasainen paikallisten kuormien jakautuminen kiinnittimien välillä.

Työn tavoitteena on kehittää jatkuvan rajapintavaurion simulointiprosessi kvasistaattisesti kuormitettujen liimalla vahvistettujen kitkarajapintojen lujuusanalysointia varten. Tuloksina esitetään sekä numeerinen mallinnusprosessi että uusia materiaaliparametrejä aikaisempaa optimaalisempien monikiinnitinliitoksilla koottavien rakenteiden suunnittelua varten.

Avainsanat Koheesiomallinnus, vauriomekaniikka, geometrinen optimointi, rajapintamurtuma

ISBN (painettu) 978-952-60-4304-3 **ISBN (pdf)** 978-952-60-4305-0

ISSN-L 1799-4934 **ISSN (painettu)** 1799-4934 **ISSN (pdf)** 1799-4942

Julkaisupaikka Espoo **Painopaikka** Helsinki **Vuosi** 2011

Sivumäärä 107 **Luettavissa verkossa osoitteessa** http://lib.tkk.fi/Diss/

Preface

The research work reported in this dissertation was initiated in 2007 at Lappeenranta University of Technology under the guidance of Professor Gary Marquis and completed during the period 2009 - 2011 at Aalto University. I am grateful to Professor Gary Marquis for instruction, supervision and his help in developing the scientific aspects of the research.

It has been an honour to have Professor Alessandro Pirondi from University of Parma and Professor Zhiliang Zhang from Norwegian University of Science and Technology as the preliminary examiners of this thesis.

I would like to thank all people who contributed this thesis. Especially, the anonymous reviewers of the international journals provided valuable comments and criticism that both significantly improved quality and guided progress of my research work. Special thanks are due to our laboratory engineer Seppo Meriläinen who did the detail design of the testing equipment used in this study. I would also like to thank Prof. Timo Björk, Dr. Pasi Tanskanen and DI Susanna Hurme for their contribution to the published articles. DI Markus Suomi from Aalto University is acknowledged for an expertise with microscopic examinations.

Financial support for this thesis was mainly granted by the Finnish National Graduate School in Engineering Mechanics. Support for some experimental aspects of the work have been provided by the LIGHT research programme of the Finnish Metals and Engineering Competence Cluster (FIMECC) and Finnish Funding Agency for Technology and Innovation (TEKES). Additional support and funding was provided by the Association of Finnish Steel and Metal Producers, Finnish Cultural Foundation, Finnish Foundation for Technology Promotion, Lempi Tammilehto Foundation, Research Foundation of Helsinki University of Technology, Research Foundation of Lappeenranta University of Technology, Ruukki Oyj, V.A. Kotilainen Foundation and Walter Ahlström Foundation. Use of the ABAQUS software was enabled via the license of the CSC – IT Center for Science Ltd.

Helsinki, June 2011 Ahti Oinonen

Contents

Nomenclature

Scalars

d	damage parameter
h, l	overlap height and length between the bracket and plate
q	uniform normal pressure due to the axial clamping load
r	radius measured from the hole centre
r_a	outer limit radius of the annular interface
r_b	inner limit radius of the annular interface, i.e. the radius of bolt through holes
r_c	average outer limit radius of the flow of uncured adhesive
r_w	outer radius of the washer
s	pitch constraint, i.e. minimum distance between fasteners
t_i	traction stress of the *i*th mode at the decohesion interface
t_i^c	critical decohesion stress
t_i^p	peak value of the traction stress
t_i^r	residual value of the traction stress due to steady friction
x_i^1, x_i^2	horizontal and vertical coordinates of the *i*th fastener
z	number of fasteners
α, β	non-dimensional shape exponents (interface constants)
γ, χ	non-dimensional shape scale parameters (interface constants)
δ_i	relative displacement of the *i*th mode at the decohesion interface
δ_i^c	critical relative displacement
δ_i^∞	relative displacement corresponding to full interface damage
δ_{eff}	effective relative displacement
ε_i	nominal strain of the *i*th mode
κ_{II}	evaluated tangential stiffness of the contact interface
μ_p	slip coefficient corresponding to the peak load
μ_r	slip coefficient corresponding to the residual shear stress
σ_2, σ_3	normal stress at the friction interface for 2D, and 3D cases

τ_{cr} slip critical shear stress

τ_{eq} equivalent friction stress

τ_{II} total shear stress at the contact surface

τ_{II}^{c} critical value of the total shear stress

τ_{II}^{p} peak value of the total shear stress

τ_1, τ_2 shear stresses at the contact surface

Δ resulted relative displacement at the interface due to applied loading

$\dot{\Delta}$ relative velocity due to applied loading

$\widetilde{\Delta}$ total relative displacement including elongation of the plate members

A pre-stress dependency slope

B pre-stress independent portion of the interfacial shear stress

G_i *i*th component of the fracture energy release rate

G_i^c critical fracture energy release rate

K_{ii} penalty stiffness of the *i*th mode

P_f pre-load of the fastener

P_p attained maximum shear force of the lap-joint

T_c constitutive thickness of the decohesion interface

T_g geometric (real) thickness of the decohesion interface

Q_f objective function, i.e. the sum of magnitudes of shear force on all fasteners

Array quantities

$\boldsymbol{e}_1, \boldsymbol{e}_2$ unit vectors in the domain plane

$\boldsymbol{m}$ moment caused by the eccentricity of the joint with respect to the centroid

$\boldsymbol{m}^i$ reaction moment from the *i*th fastener

$\boldsymbol{m}_r$ total reaction moment from all fasteners in the system

$\boldsymbol{p}$ applied shear load

$\boldsymbol{q}^i$ total shear load of the *i*th fastener

$\boldsymbol{q}_m^i$ moment-reaction component of the shear force vector

$\boldsymbol{q}_p^i$ direct load reaction component of the shear force vector

$\boldsymbol{r}_a$ eccentricity of the applied loading

$\boldsymbol{r}_b$	eccentricity of the instantaneous centre of the rotation
$\boldsymbol{r}_c^i$	distance from instantaneous centre to the *i*th fastener
$\boldsymbol{t}$	nominal traction stress
$\boldsymbol{x}^i$	position of the *i*th fastener with respect to the centroid of the pattern
$\boldsymbol{\varepsilon}$	nominal strain
$\boldsymbol{\delta}$	effective displacement
$\boldsymbol{D}$	damage matrix
$\boldsymbol{I}$	identity matrix
$\boldsymbol{K}$	constitutive matrix

Abbreviations

CZM	cohesive zone model/modelling
DCM	displacement compatibility method
FEM	finite element method
FEA	finite element analysis
ENF	end notched flexure specimen
HSS	high strength steel
IC	instantaneous centre
ID	identification
SQP	sequential quadratic programming
2D	two dimensional
3D	three dimensional

Mathematical notation

$\forall$	for all
$\in$	belongs to
$\lvert\ \rvert$	absolute value
$\lVert\ \rVert$	Euclidean norm
(a,b)	open interval

$[a,b)$	half-closed interval
$[a,b]$	closed interval
$\langle\ \rangle$	Macaulay brackets
$\times$	vector product
∞	infinity
exp	exponential function
D	domain

Original features

Previous developments of cohesive zone modelling (CZM) have mainly been concentrated with interface debonding problems and ductile fracture. Basic instrumented experiments on friction connections were performed already in the 1950s and adapted to computational mechanics in the 1980s and 1990s. In this thesis, new experimental data on combined decohesive and frictional behaviour of adhesive reinforced interfaces is produced and adapted to computational mechanics using CZM and non-local friction laws. The research results presented in this thesis have been performed during the period 2007 - 2011 and many of the main findings have been published in three conference and four journal publications. The author was the main author in five of these publications and has been responsible for oversight of all experimental work, analysis of the test results, numerical modelling and development of the theory presented in this thesis. Prof. Gary Marquis stimulated the initial research ideas and contributed the research work with valuable corrections, improvements and suggestions. The following results and features of this dissertation are considered to be original.

1. The high strength steel (HSS) specimens were used to experimentally assess the quasi-static shear strength of the epoxy adhesive reinforced frictional connection interfaces. The influence of the pre-stress, contact surface roughness and adhesive curing temperature on the shear stress vs. relative displacement response has been reported.
2. Reinforced interfaces with various normal pre-stress values have been characterized based on the predominant shear fracture behaviour, i.e. brittle, semi-brittle or ductile. Qualitative observations of the damage mechanisms, i.e. decohesion or adhesion failure, have been made.
3. Previously published shear decohesion models were examined and a new parametric damage evolution model for shear decohesion analysis of combined clamped and adhesive reinforced interfaces was developed based on the experimentally observed degradation responses. Interface constants for the

damage evolution model are fitted based on the least squares method. The suggested non-local degradation model takes into account the influence of the constant normal pressure on the shear stress vs. relative displacement response.

4. A damage function applicable for CZM is derived based on the damage evolution model. This parametric damage function enables straightforward incorporation of CZM in the finite element method (FEM).
5. Interfacial energy dissipation contributions due to the shear fracture potential and steady sliding friction are separated, i.e. the principle of superposition is applied in the characterization of the total responses.
6. The damage simulation procedure for CZM of adhesive reinforced frictional connections was numerically assessed using two dimensional (2D) FE analyses. The results of these simulations are presented for a typical test problem in which the damageable interface was modelled using decohesion finite elements. The non-local friction law was also incorporated into the interaction between the contacting elements.
7. The quasi-static tests on the full-scale double lap-joints have been performed and reported. These connections involved epoxy reinforced HSS interfaces tightened using the instrumented and calibrated HS bolts.
8. The FEM based computational damage simulation procedure developed for 2D was applied to the full-scale double lap-joint experiments. Shear fracture of the pre-defined and closed annular interface areas in the vicinity of the fasteners was modelled using decohesion finite elements involving the parametric CZM. Parameters for the CZM were taken from the simple “napkin ring” specimens.
9. A comparison of the test and computed results on the multi-fastener double lap-joints showed a good agreement. Therefore, the presented modelling procedure can be suggested to be used for engineering of adhesive reinforced connection interfaces involving friction.
10. A computationally efficient fastener layout optimization problem is formulated and programmed based on constrained geometric optimization. The equations of the classical vector superposition analysis are derived in a vector calculus form.

The representation is particularly suitable for mathematical programming and computing.

11. An eccentrically shear loaded multi-fastener bracket-to-beam connection was numerically assessed as an example structure subject to geometry optimization. An arc-shaped fastener pattern was found as an exactly equally loaded structure based on the vector sum analysis.

1 Introduction

Light and efficient solutions provide great potential for saving raw materials and energy and decreasing CO_2 emissions over the lifetime of cars, trucks and forest machinery. Therefore, many industrial sectors are pursuing improved strength-to-weight ratios especially for dynamically loaded structural applications. Designers of lifting, hoisting and transportation equipment are increasingly selecting steels with yield strengths up to 1000 MPa in an effort to reduce weight. Increased performance is an additional benefit, for example, in lifting and transport equipment. These engineering products typically include a considerable number of welded and/or bolted connections.

In the development of modern high strength steels (HSS), considerable effort has been expended to achieve high yield and fracture strength levels in combination with good surface properties and weldability. For end users and design engineers, however, the service life of a structure is frequently limited due to low fatigue strength of joints. The fatigue strength in the vicinity of structural joints is controlled by local stresses (Gough 1924; Reemsnyder 1996). As material thickness is decreased and nominal stresses increase, greater attention must be given to design details and the fatigue strength of structures that include welding can become even more critical. In general, the fatigue of welded steel structures is assessed without any advantage granted for the use of HSS (Hobbacher 2007). As a consequence, the improved fatigue life of joints still continues to be a primary challenge for the design of load carrying structures in HSS. It is a major challenge to obtain functional and safe products with extended service life which combine new materials and advanced joining methods. Optimized design methods for structures which include both the influence of the advanced materials and the influence of fabrication processes must be continuously developed.

In mechanical engineering, the finite element method (FEM) has been adapted as a standard strength analysis tool for both static and dynamic design problems. Increased computation capacity and continuous development of commercial FE programs has made it possible to perform more and more complex simulations involving e.g. frictional body contacts and damage mechanics (Zhong 1993; Belytschko et al. 2001).

An extensive literature research showed, however, that only very limited amount of input data such as material constants exists for strength analysis of adhesive reinforced frictional joint interfaces.

At Aalto University, adhesive reinforced frictional connections are currently being studied as an alternative joining method for thin sheet structures in HSS (Oinonen and Marquis 2009, 2010, 2011a, 2011b; Hurme et al. 2011). The long-term goal of the research programme is to better understand and develop design methods for adhesive reinforced frictional joints in HSS. Developing a fundamental understanding of the quasi-static strength properties is an essential first step toward understanding the fatigue strength which is low for joints produced via welding. In the context of this thesis, "thin" refers to HSS products from 3 to 8 mm in thickness. Studies concerned with interfaces involving the combination of the structural adhesive and different surface abrasion finishes in HSS have been initiated. An optimization formulation has been developed in order to reduce concentrated stress in multi-fastener connections. In this thesis, both the fundamental material property data and numerical modelling procedure for a design of structures involving adhesive reinforced multi-fastener layouts are addressed. The work concerned with the quasi-static shear loading is reported (Oinonen and Marquis 2009, 2010, 2011a, 2011b).

1.1 Background

Previous studies of cyclically loaded specimens assembled using bolts or rivets have been performed by Hansen (1959), Birkemoe and Srinivasan (1971), Reemsnyder (1975) and reviewed by Kulak et al. (1987). It has been shown that fatigue cracks develop in the material near the connection if the loading exceeds the frictional resistance capacity of the joint. In this case a serviceability limit state of slip-resistance for connections would be suitable for fatigue critical applications (Galambos et al. 1982; SFS-ENV 1993). For multi-fastener joints, joint slippage which results in bearing contact between a single fastener and plates would be sufficient to lead to fatigue failure of the structure (Hansen 1959). Correspondingly, the ultimate limit state of the connection is reached, when the maximum load-carrying capacity of the most critical

fastener within the layout has been exceeded (Galambos et al. 1982; Rutenberg 1984; Kulak et al. 1987).

A development of adhesive bonding technology has led to the use of structural adhesives in load-bearing joints in civil engineering applications such as buildings and bridges (Adams and Wake 1984; Mays and Hutchinson 1992; Gresnigt and Stark 1995). In certain repair applications, the use of adhesives can provide more convenient, faster and less expensive joint than traditional methods, e.g. welding (Mays and Hutchinson 1992; Chan and Vedhagiri 2001). Furthermore, joining of structural members in steel by adhesive bonding has been motivated by the desire to improve the fatigue strength of traditional bolted or welded connections and to prevent structural distortion due to the welding process (Mays and Hutchinson 1992). Adhesives have been used successfully to fill the clearance between the fastener and hole in reinforcement and repair operations of existing bolted connections in steel and thus improve the fatigue strength of the structure (Gresnigt and Stark 1995). In such cases, adhesive bonding increases the static shear capacity of a bolted joint up to slippage. Ali et al. (2007) have investigated fatigue properties of thin galvanized steel plates joined by epoxy bonding with comparison to the non-bonded rivet and screw joints. The endurance limit in terms of stress of the rivet and screw joints was found to be only half of the corresponding quantity obtained for the bonded lap-joints. Weld bonding, which combines spot or laser welding in conjunction with adhesives, is extensively used e.g. to join thin automotive body structures (Fays 2003).

Reinforced joints consisting of combination of mechanical fastening and adhesive bonding have been studied in the context of the light weight aeronautical structures (Hart-Smith 1985; Mann et al. 1985; Paroissien et al. 2007), composites (Chan and Vedhagiri 2001; Kelly 2005) and steel specimens (Albrecht and Sahli 1986, 1988; Imanaka et al. 1993; Oinonen and Marquis 2009; Pirondi and Moroni 2009). It has been shown that adhesive reinforcement significantly increases the quasi-static peak shear stress of lap steel connections as compared with the similar non-bonded specimens (Oinonen and Marquis 2009; Pirondi and Moroni 2009). In addition, the fatigue life of the reinforced riveted HSS joints has been found to increase with the use of epoxy adhesive (Imanaka et al. 1993). For bolted HSS sheets, there exists even the greater

strength potential due to utilization of considerably higher clamping loads as compared to e.g. riveted composite plates.

FEM is an efficient tool for strength assessment of fastener groups. However, due to the required computational resources, FEM based design optimization is not ideally suited for the optimization of fastener patterns. Numerous models with different fastener pattern variations would need to be solved and assessed. Therefore, optimization procedures which provide reasonable modelling and computing costs should be employed (Oinonen et al. 2010). Finite element analysis (FEA) can, of course, be used to assess shear load distribution for the resulting fastener pattern.

1.2 State of the art

Only a limited amount of published research exists on the theme of adhesive reinforced frictional interfaces involving higher clamping pressures which are characteristic of bolted steel connections. The quasi-static results presented in this thesis provide fundamental data for the future development of fatigue assessment methods of adhesive reinforced frictional joints. An assessment of fatigue and cyclic slip behaviour of the identical reinforced specimens has already been published by Renvall et al. (2010) and Hurme et al. (2011).

1.2.1 Testing of mechanical properties

For reinforced frictional connections, mechanical fastening provides high slip-resistance in shear (mode II) and helps to prevent peeling (mode I) failures of the adhesive. The internal strength, i.e. cohesion of the hardened adhesive material, increases the maximum shear strength of the joint interface. Furthermore, in the case of reinforced HSS joints, the relatively low Young's modulus of the adhesive increases local flexibility of the mechanically connected interface and thus reduces stress concentration between the higher modulus adherents.

Typically, the shear deformation and fracture of structural adhesives which are subjected to large-scale yielding is assessed as a function of the bond layer thickness and test temperature using the napkin ring specimens (De Bruyne 1962; Chai 2004).

This testing procedure consists of applying equal and opposite torque to two tubular adherents butt joined by an adhesive layer with a pre-defined thickness (De Bruyne 1962). The test method produces a relatively uniform shear stress distribution within the adhesive due to the continuous surface and small difference between the inner and outer diameter of the specimen (Kinloch 1987). However, due to the relatively expensive specimen fabrication and complex experimental setup of the napkin ring test, a thick-adherent lap-shear specimen has been widely adapted as a standard for determining stress-strain behaviour of adhesives loaded in shear (ASTM International 2009). Kinloch (1987) has provided a review on suggested specimens and testing procedures for structural adhesives.

Dragoni and Mauri (2000, 2002) have investigated the maximum shear strength of reinforced clamped interfaces using napkin ring specimens which were subject to torsion loading. Sawa et al. (2001) have performed similar studies. Tests involving ground contact surfaces and strong anaerobic adhesives (retainers) have shown that the slip torque is linearly dependent on the applied clamping pressure and that the adhesive provides a constant baseline shear strength which is independent from the applied axial clamping stress (Dragoni and Mauri 2000, 2002; Sawa et al. 2001). Therefore, the combined slipping and interface damage based shear load vs. displacement response of adhesively retained joints can be characterized based on the principle of superposition. However, the experiments on adhesives with lower strength have shown that the superposition method cannot be adapted as a general rule (Dragoni and Mauri 2002). These studies employed ground metallic surfaces and anaerobic adhesives. More recently, research results on epoxy reinforced frictional interfaces reported in this thesis have been published by Oinonen and Marquis (2011a, 2011b).

During the assembly process of adhesive reinforced joints with adherents in steel, the fasteners are tightened before the adhesive is cured (Albrecht and Sahli 1986; Dragoni and Mauri 2002; Oinonen and Marquis 2009). In such a case, the normal pressure between the plates created by the fasteners is high enough to force uncured adhesive out from the interface region and only small quantities remain to fill in the micro-volumes between the contact surfaces (Dragoni and Mauri 2000). The resulting elastic-plastic deformation of the original interface topography due to clamping is dependent on the initial surface roughness and yield limit of the adherent material (Archard 1953). Thus,

only a part of the adherent surfaces is in contact with the adhesive and metal-to-metal contact will occur adjacent to the formed micro-cavities. Therefore, an adhesive layer with a constant thickness, as is sometimes observed in adhesive joints with low clamping stress, does not provide an accurate physical assumption for reinforced joints in HSS involving high clamping stress. Nevertheless, an equivalent adhesive thickness may be adapted in computational analyses (Sawa et al. 2001). According to Archard (1957), the first relaxation of the high normal pre-stress and subsequent reloading deforms metal asperities predominantly elastically. The fundamental research work reported by Archard (1953, 1957) and Greenwood and Williamson (1966), however, exclusively addresses non-bonded contacts of rough surfaces.

During decohesive cracking, fracture energy is dissipated. For ductile and semi-ductile materials, resistance to fracture material bonds and displacement of the fracture surfaces is often described using *R*-curves, i.e. energy dissipation as a function of the extent of crack propagation (Broek 1984). In general, the *R*-curve should be determined directly from the actual energy release rate. The *R*-curve should not be used for fully brittle fracture (Bao and Suo 1992). In the cases involving unavoidable non-steady crack propagation due to a periodically brittle fracture, the effective *R*-curve (R_{eff}-curve) term can be used (Nairn 2009). Previously, the *R*-curve has been used to describe the delamination resistance of composites (Krueger et al. 2000) and fracture resistance of adhesive bonded interfaces (De Moura 2008). The analogous *G*-curves, i.e. the failure energy release rate curve for cohesive zone, have been developed for epoxy reinforced frictional HSS interfaces by Oinonen and Marquis (2011a, 2011b). For clamped interfaces, the *G*-curve directly presents the energy release rate vs. relative displacement behaviour. Particularly for the adhesive reinforced interfaces, the contribution of frictional dissipation is excluded from the *G*-curve (Oinonen and Marquis 2011a, 2011b).

The shear load carrying capacity of thermosetting epoxy adhesives has been observed to increase when the adhesive thickness is decreased (Khrulev 1965; Chai 2004). Consequently, the critical fracture energy release rate of the adhesive material has been shown to strongly decrease if the thickness of the adhesive layer is increased (Chai 1988, 2004). Therefore, bulk material properties of the cured adhesive cannot directly be adapted for use in strength assessment or in a FE model.

The effects of curing temperature on the shear strength of the adhesive bonded lap-joints have been investigated by Matsui (1990). For heat-cured epoxy adhesive joints, the results indicated a substantial increase in the average ultimate shear stress as compared to existing data from similar specimens cured at room temperature. Stewart et al. (2007) have also reported a notable increase in the lap shear strength of the epoxy adhesive joints which had undergone four hours post-curing in 40 - 90 °C.

The relationship between shear strength and surface roughness shows only a marginal decrease of 3 MPa in the maximum shear stress of the epoxy bonded lap-joint when the arithmetical mean roughness, Ra, of the surface is increased from 1 to 3 μm (Uehara and Sakurai 2002). However, it has been previously concluded that the dependency between joint strength and surface finish is a complex phenomenon and cannot be generalized for different loading conditions and materials involved (Khrulev 1965; Shahid and Hashim 2002). A very limited amount of research addresses the influence of different abrading conditions on the shear strength of combined clamped and bonded interfaces (Oinonen and Marquis 2011b).

To this end, Mengel et al. (2007) have experimentally shown that shear strength of bonded cylindrical steel-magnesium joints can be increased considerably by curing the epoxy adhesive under relatively high hydrostatic pressure, i.e. up to 100 MPa. Correspondingly, the reinforced clamped connections presumably strengthen due to the cure of adhesive under characteristically developed increased pressure in the micro-cavities during the curing process. However, it is difficult to experimentally proof and further develop interfaces in order to benefit of this strengthening effect to a higher degree. Therefore, this interesting phenomenon is left as a future note, and it is not further addressed within this thesis. In contrast, an effect of the curing temperature on the shear strength can more straightforwardly be accessed.

1.2.2 Modelling of interfacial slip and damage

In computational mechanics, frictional mechanisms are classified as quasi-static, dynamic or wear damaging (Oden and Martins 1985). For dynamic friction, penetration and plastic deformation of the interface is assumed not to occur. Surface roughness has been found to influence the stiffness of the contacting interfaces (Oden and Martins

1985). Additionally, the dynamic friction coefficient has been found to depend on the slip rate, i.e. the relative sliding velocity of the surfaces (Richardson and Nolle 1976). For many quasi-static engineering applications, however, the slip velocity is low enough for the rate dependency of the friction coefficient to be ignored (Oden and Martins 1985). Frictional properties of the epoxy reinforced HSS interfaces in damaged condition involving the constant slip rate has been reported by Oinonen and Marquis (2011a, 2011b).

Decohesion finite elements have been developed to provide a suitable option to simulate progressive damage of adhesive bonded interfaces (Camanho and Dávila 2001, 2002; ABAQUS Inc 2010). For a typical cohesive zone model (CZM), the magnitude of the interface traction stress increases, achieves its maximum value, and finally falls to zero due to damaging loading/displacement. In this case there is no need to define an initial crack and the damage is restricted to evolve along the pre-defined cohesive interface. Decohesion finite elements are placed between solid finite elements of the base material. Principles from fracture mechanics, such as the fracture energy release rate, can be adapted to control the separation of the interfaces. After a specified damage initiation criterion is reached, a damage evolution law begins to govern the degradation process of the interface. A damage function derived from its corresponding damage evolution law, enables incorporation of different CZMs in FEM. The most common mathematical models for CZM are either bi-linear (Dávila and Camanho 2001) or trapezoidal (Tvergaard and Hutchinson 1996). Non-linear laws for CZM have been developed e.g. by Needleman (1987), Allix et al. (1995), Valoroso and Champaney (2006) and Oinonen and Marquis (2011a). An experimentally validated CZM can be implemented in FEM and thus provide a versatile modelling approach for the more complex adhesive joining related engineering problems (Camanho et al. 2003; De Moura 2008). Previously, CZM have been adapted to model decohesion of adhesive bonded interfaces involving clamping pressure (Pirondi and Moroni 2009; Oinonen and Marquis 2009, 2011a).

The fracture energy and critical interface stress govern the strength of the interface and therefore comprise the basis for material property determination for the FE model calibration. CZM which are implemented in FEM, are exploited to determine the critical fracture energy release rates of bonded joints (De Moura and Chousal 2006). A

consistently determined R_{eff}-curve, or analogously G_{eff}-curve, can be regarded as a mechanical property and it additionally provides an appropriate theoretical connection with the corresponding CZM (Nairn 2009).

Recently, Oinonen and Marquis (2009, 2011a, 2011b) have suggested a modelling procedure that includes both the cohesive and frictional properties at the clamped joint interface. The process allows a physical characterization of the energy dissipation contributions due to the interfacial shear fracture potential and non-local friction separately at the contact. Consequently, the principle of superposition can applied in the determination of the total responses. Hence, the suggested modelling principle is particularly suitable for damage simulation of adhesively retained non-slip bolted joints involving high contact pressures. Furthermore, if applicable, all existing friction laws can be included in the FE contact involving CZM. The contribution of friction is excluded from the CZM (Oinonen and Marquis 2011a).

1.2.3 Design of non-slip multi-fastener connections

In order to improve static strength, slip resistant bolted joints in structural steel with adhesive reinforced lap interfaces have been introduced by Albrecht and Sahli (1988). For example, in highway bridge applications reinforcement bonding is made using two-component epoxy (Gresnigt and Stark 1995) or acrylic (Albrecht and Sahli 1986, 1988) adhesives with high elastic modulus. The reinforcement carries most of the shear load but if the interface fails, bolts will carry the quasi-static load in bearing thus providing for safer operation. Improving quasi-static slip resistance of bolted lap-joints using structural adhesive reinforcement has consequently been shown to increase fatigue strength (Albrecht and Sahli 1986).

Strengthening structural connections in the early design process by reducing the maximum fastener loads has been focus in few optimization studies. Chickermane et al. (1999) have derived a topology optimization based approach for a search of optimal fastener locations. Oinonen et al. (2010) exploited the gradient-based sequential quadratic programming (SQP) to solve a fastener pattern optimization problem with an objective to minimize the sum of the fasteners' shear load magnitudes. An eccentrically

shear loaded multi-fastener bracket-to-beam joint was assessed as a design example subject to geometry optimization.

The computationally efficient elastic vector sum method is frequently employed in the analysis of patterns for bolting and riveting, see e.g. Salmon and Johnson (1996). Reilly (1870) and Prichard (1895) were among the first to publish applications of this engineering approach to the strength analyses of eccentrically loaded rivet groups. This method assumes that the total shear force on a fastener is the vector sum of two components. The first component is the direct shear component which acts parallel to the applied force and is equal for all fasteners in the group. The method further assumes that the moment-reaction shear force component for each fastener is proportional on the distance between the fastener and the centroid of the group and that its direction is perpendicular to the position vector of the fastener with respect to the centroid.

The instantaneous centre of rotation (IC) concept first suggested by Gullander (1914) is also widely used to calculate the shear load on fasteners within a group. In linear-elastic cases, identical results are obtained for both the vector sum and IC method. However, Muir and Thornton (2004) have shown that the equilibrium condition which satisfies the load-deformation relationship of the fastener group with the IC concept can only be obtained if a linear-elastic constitutive model is assumed and if the load is perpendicular to the symmetry axis of the fastener pattern. This limitation is due to the inherent discontinuity in the equilibrium equations which would exist if the fasteners' loads are assumed to equalize due to slipping or yielding.

The displacement compatibility method (DCM) developed by Swift (1984) provides an efficient procedure for the evaluation of fastener loads on both cracked and uncracked stiffened panels. The gain in computation time of DCM is based on the exploitation of exact analytical solutions for the displacements and stress intensity factor. In addition, an advantage of DCM over the vector superposition and IC methods is that the elastic behaviour of the plate and flexibility of the fasteners can be taken into account. Although DCM is fundamentally a general approach, its application will be limited to certain well defined cases where analytical solutions for displacement and stress intensity factors are known, e.g. when an infinite plate is subjected to a tensile load. It is difficult to adapt DCM to the analysis of eccentrically loaded multi-fastener joints.

1.3 Applicability, limitations and requirements

The fracture and strength assessment reported in this thesis can be assumed to provide an input for design data and improve a modelling accuracy of both the epoxy reinforced and non-bonded frictional HSS interfaces with different surface roughness. The suggested modelling procedure is applicable to FEM based quasi-static simulation of combined interfacial fracture and slip, e.g. an assessment of the serviceability limit state of non-slip bolted connections. Engineering problems involving reinforced HSS interfaces have not previously been widely studied and thus, some characteristics still lack experimental validation. Therefore, some necessary assumptions and simplifications have been made within this study. These aspects, important notes and further limitations are discussed below.

Adhesive reinforced clamped interfaces were tested using a constant shear displacement velocity. The simulation models involving the parametric CZM are thus adjusted to this slip rate. Characteristically, unavoidable periodically brittle shear fracture behaviour of some interfaces was experimentally observed; especially for the heat-cured interfaces. The related rate dependency of interfacial degradation was beyond the scope of this study and lacks experimental data. This complex dynamic phenomenon was also beyond the scope of the modelling. Wear of abraded HSS due to sliding under significant normal pressure is taken into account by CZM, but it is not separated from the total damage behaviour of interfaces. Although heat generation is closely related to friction, it is excluded from this thesis due to the low displacement velocities used. Heat rise in the specimens was not noticeable and is assumed as low enough for its influence on the results to be negligible.

Characteristic fracture behaviour of the pre-stressed reinforced interfaces has previously been shown to depend on the adhesive type (Dragoni and Mauri 2002). With structural applications in mind, a two-component epoxy adhesive with the high stiffness and good resistance to increased ambient temperatures was used for reinforcing the HSS interfaces (3M United Kingdom PLC 2001). Additional adhesive types and/or environmental effects on adhesives are not covered within the current study. The characteristics such as ageing and creep behaviour should be assessed before applying

the reported results in different working conditions. See e.g. the current work reported by Doyle and Pethrick (2009).

All performed experiments and computations are limited to shear damage scenarios where the joint interface has been cured under clamping without other external loads involved. However, the interfaces of the tested full-scale joints are influenced due to an effect of the applied direct shear load on the normal stress distribution field, i.e. shear lag in the lap-joints necessarily causes changes in the normal stress distribution near the fastener. Hence, the normal pre-stress varies before shear damage initiation. This effect has not yet been validated using the simple napkin ring test specimens which had near perfect boundary conditions. For this reason, the corresponding three dimensional (3D) simulations were computed using a CZM with an averaged critical shear stress value within decohesion interface areas. Due to experimentally observed brittle fracture behaviour, exclusively the computed maximum static shear load carrying capacity of the adhesive reinforced full-scale joints has been validated.

The computational cost of FEM based damage simulations is not addressed within this thesis. To reduce the computational cost of the simulations using CZM it is necessary to investigate how to solve the convergence problems that appear with implicit, such as Newton-Raphson, solution methods (Turon et al. 2006). The adapted FE mesh size was based on the fact that the results did not noticeably change if the smaller element size was used in the trial simulations. Therefore, the presented results can be assumed as converged.

The solved geometry optimization problem resulted to an arc-shaped fastener pattern which is based on the widely used vector sum method (Reilly 1870; Kuzmanović and Willems 1977; Salmon and Johnson 1996). The vector sum method relies on the engineering assumptions (Muir and Thornton 2004) and the obtained fastener pattern may, in specific cases, require further assessment by FEM (Oinonen et al. 2010). For most applications, the resulting layout efficiently provides a close estimate of the most optimal fastener pattern.

In summary, this thesis is concentrated with the development of the methods for design of more optimal engineering structures involving adhesive reinforced non-slip

multi-fastener connections. The essential requirements for the theory are the following items.

1. The parameters of the damage evolution model should be identified based on the fundamental experiments in order to ensure a sufficient accuracy and validation of the FEM based simulation models.
2. The experimental programme should include different abrasion finishes, i.e. ground and grit blasted surfaces. These are typical surface conditions in engineering applications, e.g. bolted non-slip connections (Kulak et al. 1987).
3. A strength effect of the reinforcement bonding is shown by comparing the test results of the bonded interfaces to the identical experiments based on the non-bonded specimens. This applies for both the fundamental experiments and tests on the bolted lap-joint specimens.
4. The developed modelling process should separate the energy dissipation contributions due to sliding friction and degradation of the interface. This requirement indicates that a fully damaged interface exclusively involves frictional properties.
5. The solution of the interface damage response should parametrically include the influence of the constant normal stress on the total shear stress vs. displacement response of the interface.
6. The suggested damage modelling procedure involving CZM can be implemented in FEM. The FEM based 2D test model can be generalized to 3D interface damage simulations on the full-scale bolted/bonded connections.
7. A development of the computationally efficient geometric fastener layout optimization problem is presented. The main requirement is that the shear load in the most severely loaded fastener in the group is reduced in order to more uniformly distribute the resultant shear loads between the fasteners.

2 Experimental determination of quasi-static response

An experimental programme was initiated to determine the interface shear stress vs. relative displacement curves for reinforced and non-bonded clamped interfaces. The results obtained from the specimens with the highly abraded (grit blasted) contact surfaces are compared with the identical loading cases involving considerably smoother (ground) contact surfaces. The effect of curing temperature was investigated by comparison of the results based on the specimens cured at room temperature to the identical cases involving heat cure.

The observed predominant shear fracture behaviour, i.e. brittle, semi-brittle or ductile, under different clamping pressure and abrasion conditions is characterized based on the experimental observation. Observations are also made on the damage mechanisms, i.e. decohesion or adhesion failure. Selected photographs of both the bond lines of the non-damaged interfaces under clamping and fracture surfaces of the damaged interfaces are presented. There is also a summary of the peak values of the evaluated shear stress at the interfaces. Parametric fits of the measured total interface shear stress vs. relative displacement responses are calculated for the grit blasted contact surfaces. In Section 3, these results are exploited in a development of the computational damage modelling procedure.

2.1 Specimens with axial pre-stress

The clamped application of specimens of napkin ring type (De Bruyne 1962) was adapted for all fundamental experiments of the current study. This specimen type has the advantageous characteristics to the napkin ring, and axial clamping load could be applied without disturbing the tangential shear stress uniformity. Test specimens were machined from HSS sheets with a nominal yield strength of 960 MPa. The design and dimensional details of the specimen are given in Figure 1. The eight threaded holes were used for fixing the specimens into the testing device.

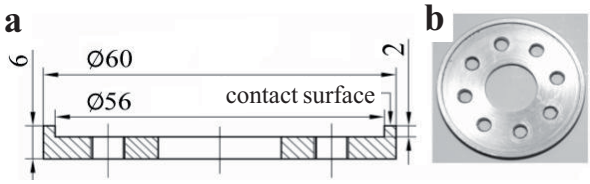

Figure 1. a) Test specimen with the main dimensions [mm]. b) Photograph of the specimen.

2.1.1 Preparation, bonding and cure of interfaces

Grit blasted, coarse ground and fine ground contact surfaces were investigated. Surface roughness following abrading was measured in the circumferential direction from the sixteen randomly selected locations for each of the surface types. The gauge length of each measurement was 2.5 mm. The average arithmetical mean roughness (Ra), maximum peak (Ry) and ten-point mean roughness (Rz) are presented in Table 1. An example of the typical profile of a grit blasted contact surface is shown in Figure 2.

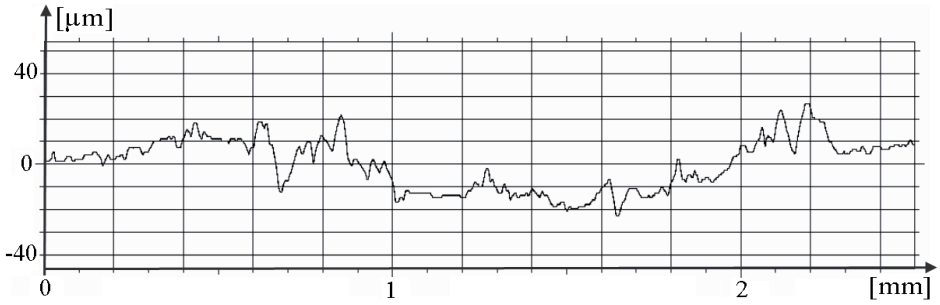

Figure 2. Typical surface profile vs. measuring distance (2.5 mm in total) of the grit blasted surface before the clamping and testing procedure (produced using the TalyProfile 3.2.0 program).

Table 1. Measured contact surface roughness [μm].

Surface type	Ra	Rz	Ry
Fine ground	0.38	2.02	3.42
Coarse ground	0.57	3.26	5.34
Grit (aluminium oxide) blasted	3.57	22.42	31.21

A two-component structural epoxy adhesive DP760 produced by 3M was used for all reinforced interface configurations (3M United Kingdom PLC 2001). All circular contact surfaces were cleaned with pure acetone to ensure proper adhesion (Wegman 1989). The surfaces inside of the (ϕ = 56 mm) contact area (Figure 1) were protected using an O-ring seal to prevent adhesion inside the desired contact areas and to reduce the build-up of an inner spew fillet. During the assembly process, adhesive was exclusively applied to the contact surfaces of the specimens, and clamping to the desired pre-stress was immediately applied. The outer surfaces of the specimens were cleaned of excess uncured adhesive. For reference, the mechanical properties of the epoxy adhesive reported by the manufacturer are given in Table 2. Differently from the present study, the limit stress data presented in Table 2 is based on overlap shear specimens in aluminium and 150 μm glue line thickness.

Table 2. Mechanical properties of the structural epoxy adhesive DP760 based on the test method EN 2243-1 (3M United Kingdom PLC 2001).

Cure conditions	Shear strength [MPa]	Young's modulus [MPa]
7 days at 23±2 °C	28.2	5972
2 hours at 65±3 °C	29.1	not reported

The pre-defined clamping stress was constant during the curing process, and it was not released before the subsequent testing was performed with the same stress. Five different axial pre-load values, q = {4,50,100,150,200} MPa, were considered for each of the surface finish variations. The value q = 4 MPa corresponded to the lowest pressure needed to force uncured adhesive out from the interface region and to firmly close the contact.

The heat cure of adhesive was performed at 65±3 °C for two hours. The heat-up time from 20 to 65 °C was 2½ hours. The other studied cure method involved hardening at room temperature, i.e. 20±1 °C for one week (3M United Kingdom PLC 2001).

2.1.2 Micro-sections of bond-line

The bond lines of the contact interfaces are shown in Figure 3 for each studied surface type and for q = 100 MPa. The identifiable magnified details from the figures on the left are shown on the right for each case. These micro-sections were produced following the previously described bonding process involving the heat cure. Constant q was developed using an instrumented bolt; it remained constant during curing, preparation and microscopic examination of the micro-section. For each of the bonded and clamped specimen pairs, approximately 1 mm of material was tangentially machined away from the outer diameter. This new surface was then polished, followed by a subsequent microscopic examination. See also Figure A5a in Appendix A.

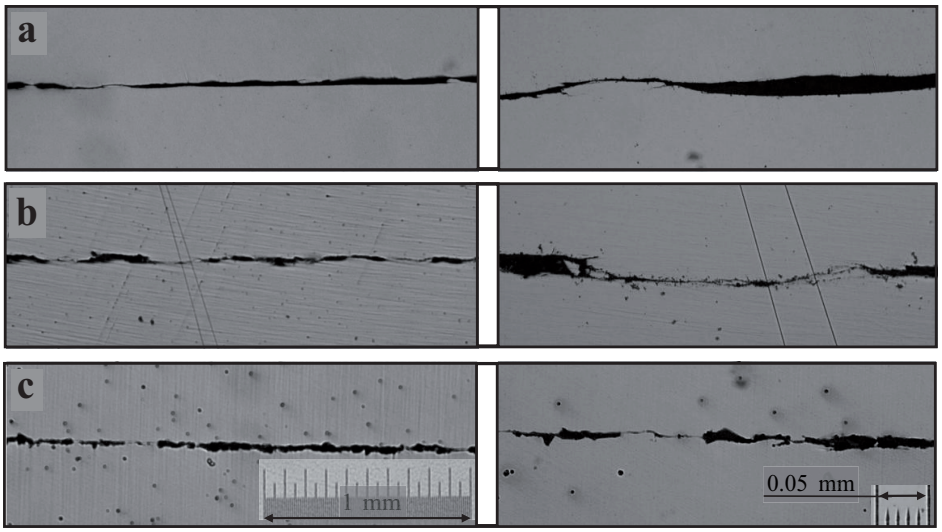

Figure 3. Polished micro-sections of the tangential bond line of the contact interfaces under the clamping load q = 100 MPa. The magnified details from the figures on the left are shown on the right for the each interface types: a) Fine ground. b) Coarse ground. c) Grit blasted.

2.2 Quasi-static testing system

For all fundamental experiments, a tailor made testing device shown in Figure 4 was used. See also Appendix A for more details presented in Figures A1-A3. The servo-hydraulic actuated test machine applied pure torsion load across the circular specimen-pair interface. During testing, normal stress on the interfaces was maintained via a threaded rod equipped with an in-line axial load cell. Normal stress was continuously measured during curing and testing, in order to verify that it varied by no more than 1 % from the desired value. The threaded rod was equipped with low friction axial thrust bearings at each end. The influence of bearing friction due to pre-load on the measured torque was less than 1.5 % for all tests. Therefore, the measured torque was assumed to be exclusively transmitted across the interface. An eddy current extensometer was fixed to each side of the specimen pairs in order to measure displacement between the contact surfaces. The static resolution and measurement precision of the eddy current sensor were better than 10.0 μm and 20 μm, respectively. Rotation displacement was applied at the nominal rate of $\dot{\Delta} \approx 0.027$ mm/s, measured at the mean diameter of the contact interfaces. However, the actual $\dot{\Delta}$ was not constant due to the unavoidable periodically semi-brittle fracture behaviour. During testing the temperature was maintained at 20±1 °C.

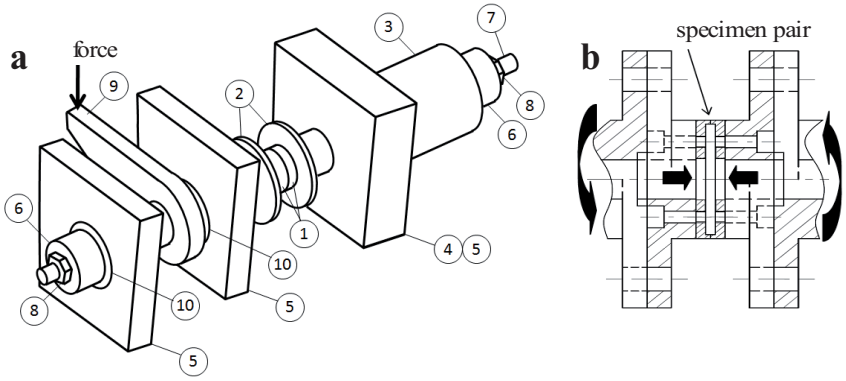

Figure 4. a) Schematic of the testing device. The key components are: (1) specimen pair, (2) specimen holders, (3) axial load cell, (4) torque reaction, (5) support, (6) thrust bearing, (7) threaded rod, (8) nut, (9) torque arm, and (10) rotation bearing. b) Detailed sketch with the applied direct and torsional loads.

2.3 Combined decohesion and slip

In this section, the predominant shear fracture behaviour of the epoxy reinforced HSS interfaces is characterized and the damage evolution model is developed. The maximum values of the total interface shear stress τ_{II}^{p} are presented for the studied normal pressure values, q = {4,50,100,150,200} MPa. In addition, the measured total shear stress τ_{II} vs. relative displacement Δ curves are plotted for the selected experiments. The parameters of the damage evolution model are fitted for the grit blasted cases. For $\Delta \in [1.0,3.0)$ mm, the responses of all bonded interfaces were observed to exclusively consist of steady sliding friction. Therefore, the range $\Delta \in [0,1.0]$ is considered to be of primary interest for representing the result data.

2.3.1 Predominant shear fracture behaviour and mechanism

Figure 5 shows the fully damaged contact surfaces for q = 4 and Figure 6 for q = 100 MPa, respectively. The magnifications from the figures on the left are shown on the right for all the examined surface types. Based on Figures 5a-b, the interfacial fracture mechanism was due to adhesive failure for both the fine and coarse ground interfaces. In contrast, the grit blasted interface showed predominantly cohesive failure, as indicated by Figure 5c. With reference to the surfaces shown in Figures 6a-c, a predominantly cohesive failure can be observed for all the studied interface types.

Observed predominant shear fracture behaviour is summarized in Table 3 for all the reinforced interface types involving significant pre-stress, i.e. $q \in [50,200]$. The characterization listed in Table 3 is based on the measured responses reported in Section 2.3 and Figures 5 and 6. For all interfaces stressed to q = 4, a fully brittle fracture occurred.

Table 3. Predominant shear fracture behaviour of the epoxy reinforced interfaces for the significant clamping stress range, $q \in [50,200]$ MPa (FG = fine ground, CG = coarse ground and GB = grit blasted).

Interface	Cure temp °C	Brittle	Semi-brittle	Ductile	Unstable
FG	65±3	$q \in [50,100]$	$q = 150$	$q = 200$	
FG	20±1	$q = 50$	$q = 100$	$q \in [150,200]$	
CG	65±3	$q \in [50,100]$			$q \in [150,200]$
GB	65±3		$q \in [50,150)$		$q = 200$
GB	20±1			$q \in [50,200]$	

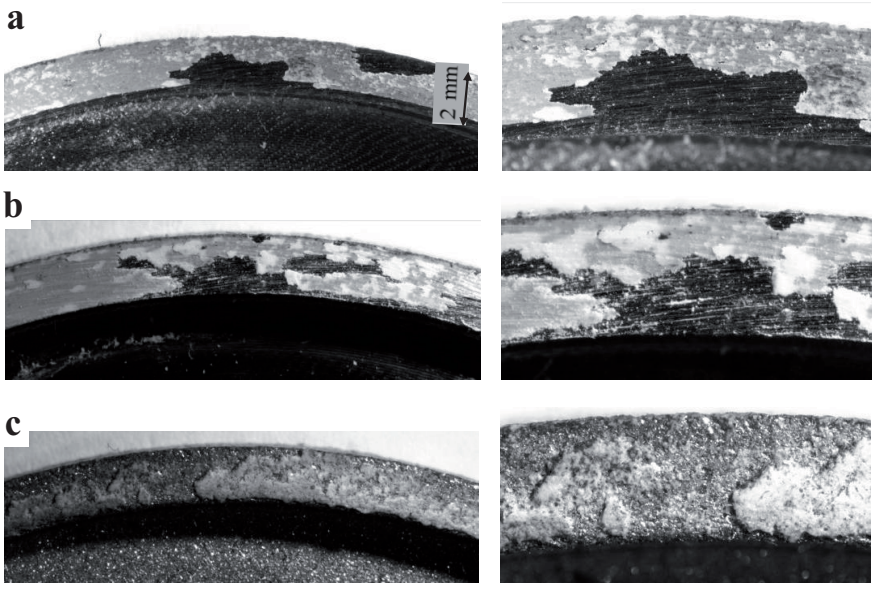

Figure 5. Contact surfaces for q = 4 MPa after the fully brittle shear fracture. The magnified details from the figures on the left are shown on the right for each of the surface types: a) Fine ground. b) Coarse ground. c) Grit blasted.

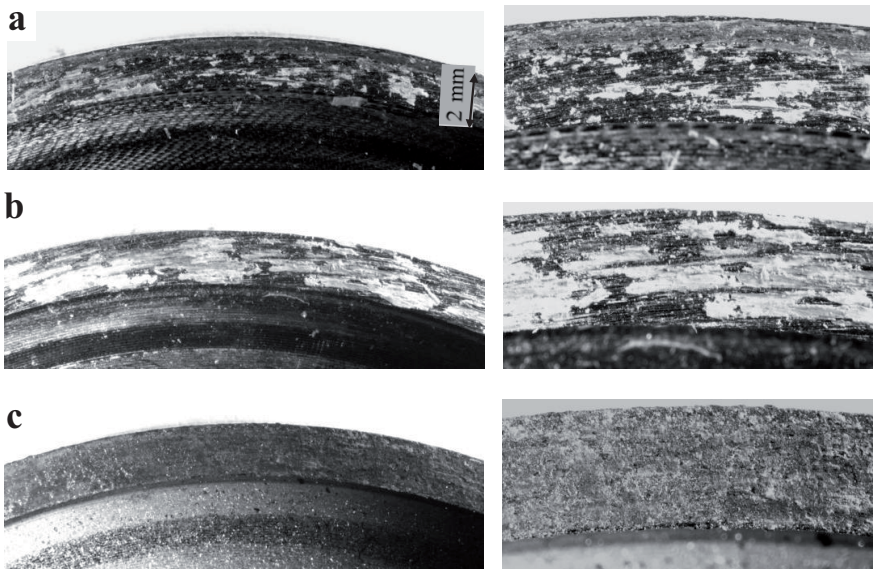

Figure 6. Damaged contact surfaces for q = 100 MPa and $\Delta \rightarrow 3.0$ mm. The magnifications from the figures on the left are shown on the right for each of the surface types: a) Fine ground. b) Coarse ground. c) Grit blasted.

2.3.2 Peak and critical shear stresses

The measured values of $\tau_{\mathrm{II}}^{p}(q)$ are summarized in Figure 7. With reference to the τ_{II} vs. Δ responses shown below in Figures 8-10, $\tau_{\mathrm{II}}^{p}(q)$ always occurred within the range $\Delta \in (0,0.15)$ mm. Figure 7 includes results from the studied surface finish variations both with and without bonding involving the significant pre-stress, i.e. $q \in [50,200]$ MPa. For the experiments involving the non-bonded ground contact surfaces, non-linear slip hardening of the interfaces was observed, as seen in Figure 16. In such cases, the critical values at the beginning of the observed slip τ_{II}^{c} are reported. The linear least squares fitting method (The MathWorks 2011a) was applied to develop the relationship between $\tau_{\mathrm{II}}^{p}, \tau_{\mathrm{II}}^{c}$ and q,

$$\tau_{\mathrm{II}}^{p}(q) = Aq + B \text{ and } \tau_{\mathrm{II}}^{c}(q) = Aq + B, \quad q \in [50,200). \tag{1}$$

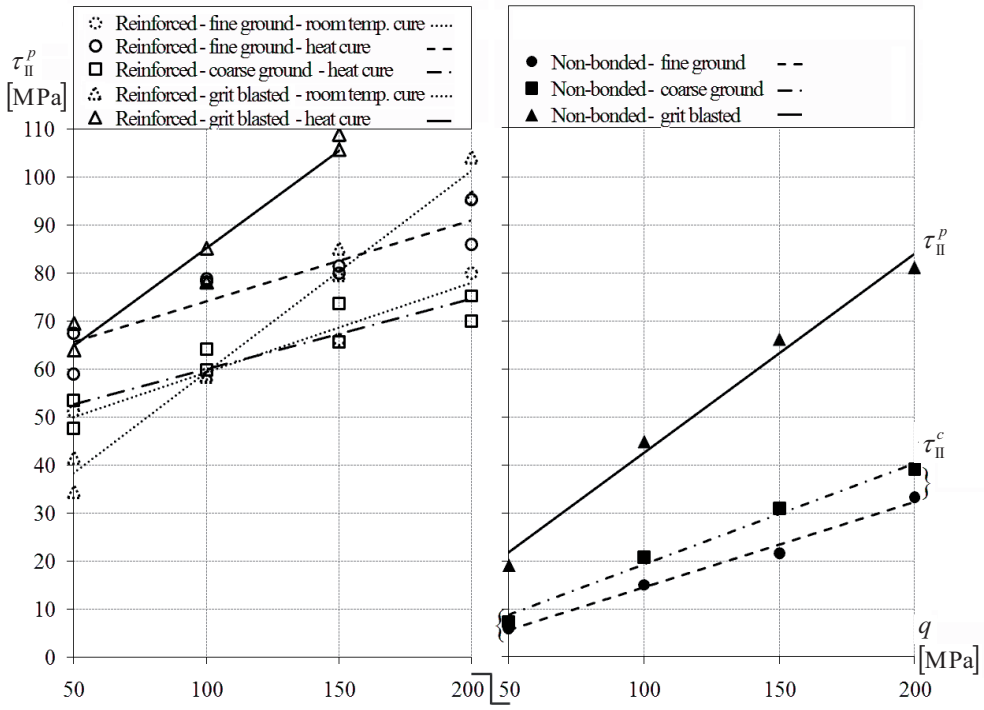

Figure 7. Peak values of the maximum measured interface shear stress τ_{II}^{p} vs. clamping stress q are shown with the corresponding linear least squares fit. The critical values τ_{II}^{c} are plotted exclusively for the non-bonded ground contact surfaces.

Eq. (1) provides an estimate for assessing $\tau_{\mathrm{II}}^{p}(q)$, $\tau_{\mathrm{II}}^{c}(q)$ within the range of $q \in [50,200)$ MPa. The calculated fitting coefficients A and B for each interface variation are given in Table 4. For q = 4 MPa, a different failure mechanism was reported in Section 2.3.1 and, therefore, the data for q = 4 was excluded from the regression fit. The values of $\tau_{\mathrm{II}}^{p}(q)$ for this case are given in Table 5.

Table 4. Matrix of experiments involving $q \in [50,200]$ MPa and the numerical values of the fitting parameters A and B for Eq. (1) (FG = fine ground, CG = coarse ground and GB = grit blasted).

Interface type	Tests for each q	Cure temp °C	A	B [MPa]
FG - bonded	2	65±3	0.169	57.23
FG - bonded	1	20±1	0.187	40.71
FG - non-bonded	1	-	0.177	-3.21
CG - bonded	2	65±3	0.147	45.35
CG - non-bonded	1	-	0.211	-1.81
GB - bonded	2	65±3	0.406	44.56
GB - bonded	2	20±1	0.421	17.22
GB - non-bonded	1	-	0.415	0.99

Table 5. Measured peak values of the interface shear stress τ_{II}^{p} [MPa] for the low pre-stress q = 4 MPa and 65±3 °C cured epoxy.

Interface type	τ_{II}^{p}, test I	τ_{II}^{p}, test II	Average τ_{II}^{p} based on the tests I and II
Fine ground	49.4	46.2	47.8
Coarse ground	49.2	43.4	46.3
Grit blasted	54.5	52.1	53.3

2.3.3 Post-peak response of adhesive reinforced ground interfaces

In Figure 8, the combined slip and interface decohesion response of the reinforced specimens with the fine ground contact surface finish is shown. Test data from the specimens cured at 65±3 °C is compared to the corresponding cases with the 20±1 °C cure. Exclusively the more conservative, i.e. lower τ_{II}^{p}, data is shown from cases where replicate tests were performed. The initial interface decohesion response of the coarse ground specimens for $\Delta \in [0,0.10]$ mm based on the experiments with q = 150 and q = 200 MPa is shown in Figure 9.

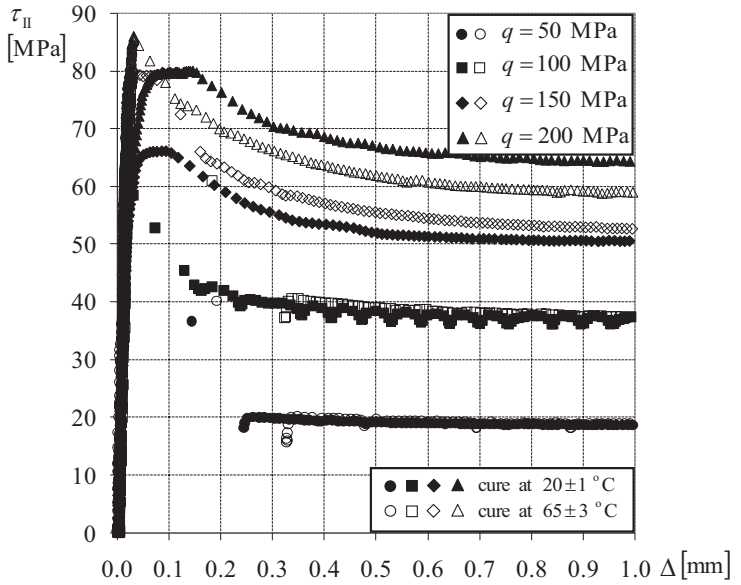

Figure 8. Combined slip and interfacial decohesion responses of the specimens with the fine ground contact surface finish. The test data of the conservative results with 65±3 °C cure is compared with the corresponding results obtained by 20±1 °C cure.

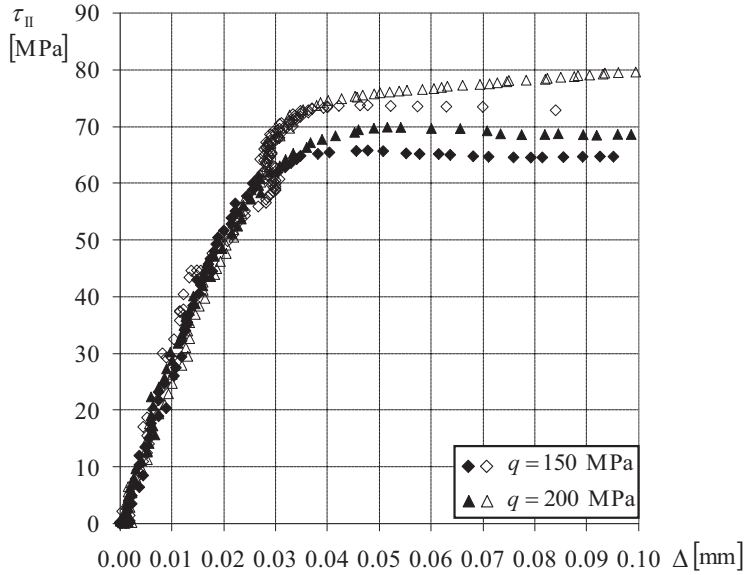

Figure 9. Initial interface decohesion response of the reinforced coarse ground specimens, the cases q = 150 and q = 200 MPa are shown.

2.3.4 Post-peak response of adhesive reinforced grit blasted interfaces

Figure 10 shows the measured $\tau_{II}(\Delta)$ response of the adhesive reinforced specimens involving 65±3 °C cure. Two tests were performed for each q, and the data shown in Figure 10 corresponds to the more conservative, i.e. lower τ_{II}^{p} of them, from the two identical experiments. The measured data for q = 200 MPa is excluded from Figure 10 due to observed incoherent and highly unstable response before attaining τ_{II}^{p} in two identically performed tests.

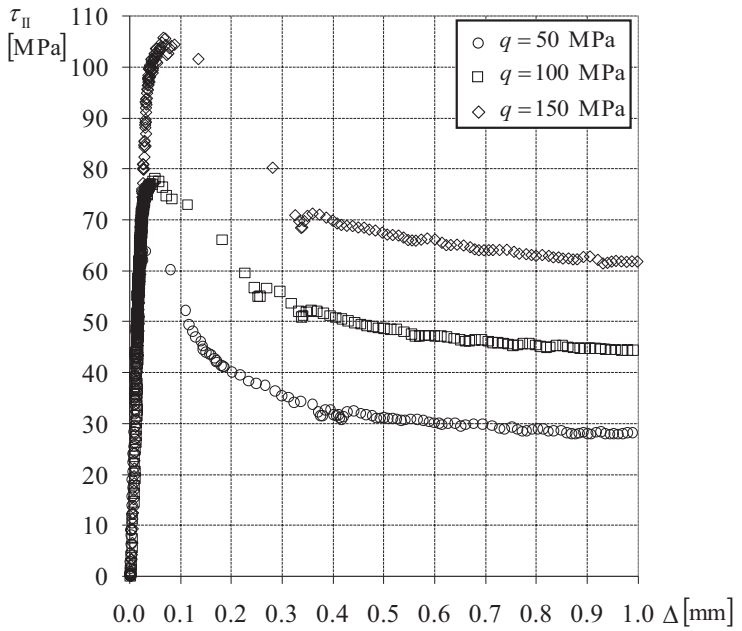

Figure 10. Combined slip and interface decohesion responses of the specimens with the grit blasted contact surface finish. The heat cure was performed at 65±3 °C for two hours.

Figure 11 shows the $\tau_{II}(\Delta)$ response of the reinforced grit blasted specimens with 20±1 °C cure. The results of the two nominally identical tests are presented.

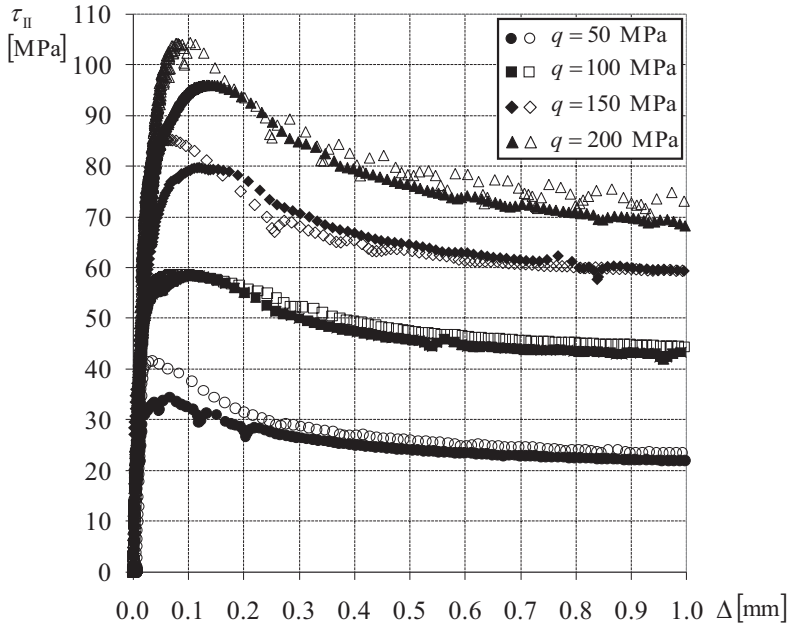

Figure 11. Combined slip and interface decohesion response of the specimens with the grit blasted contact surface finish. The room temperature cure was performed at 20±1 °C for one week. The data of two identical tests is shown and the conservative results are identified by the filled markers.

2.3.5 Model of interfacial slip and damage response

From Figures 10 and 11, the shear fracture behaviour can be characterized as shown in Figure 12. Based on the principle of superposition, the shear fracture potential of interfaces can be determined independently from the contribution of steady frictional dissipation. Eqs. (2) and (3) mathematically present the corresponding calculated total shear stress vs. relative displacement responses $t_{II}(\delta_{II})$ shown in Figures 12a and 12b, respectively. The fitting of the numerical coefficients for Eqs. (2) and (3) is described in Section 2.3.6.

$$t_{\mathrm{II}}(\delta_{\mathrm{II}}) = \begin{cases} \kappa_{\mathrm{II}}\delta_{\mathrm{II}}, & \delta_{\mathrm{II}} \in \left[0, \delta_{\mathrm{II}}^{\mathrm{c}}\right) \\ t_{\mathrm{II}}^{c}\left[\exp\left(\alpha\left(\delta_{\mathrm{II}} - \delta_{\mathrm{II}}^{c}\right)\right)\right] + t_{\mathrm{II}}^{r} & \delta_{\mathrm{II}} \in \left[\delta_{\mathrm{II}}^{\mathrm{c}}, 1.0\right] \end{cases} \tag{2}$$

$$t_{\mathrm{II}}(\delta_{\mathrm{II}}) = \begin{cases} \kappa_{\mathrm{II}}\delta_{\mathrm{II}}, & \delta_{\mathrm{II}} \in \left[0, \delta_{\mathrm{II}}^{\mathrm{c}}\right) \\ t_{\mathrm{II}}^{c}\left[\gamma\exp\left(\alpha\left(\delta_{\mathrm{II}} - \delta_{\mathrm{II}}^{c}\right)\right) + \chi\exp\left(\beta\left(\delta_{\mathrm{II}} - \delta_{\mathrm{II}}^{c}\right)\right)\right] + t_{\mathrm{II}}^{r} & \delta_{\mathrm{II}}\left[\delta_{\mathrm{II}}^{\mathrm{c}}, 1.0\right] \end{cases}. \tag{3}$$

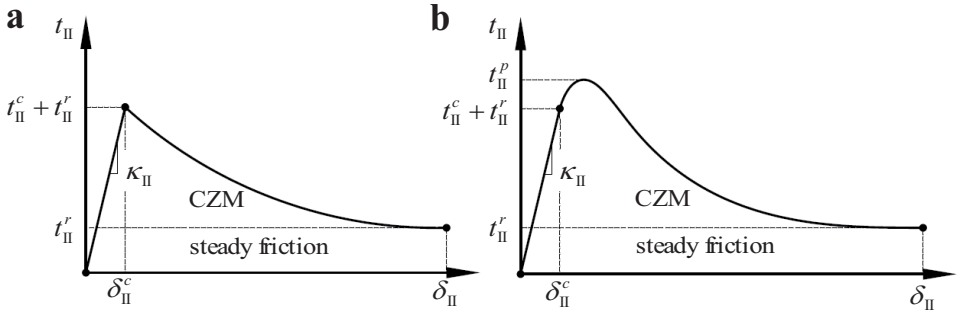

Figure 12. Models of $t_{\mathrm{II}}(\delta_{\mathrm{II}})$ response of the reinforced grit blasted HSS interfaces. a) For 65±3 °C cured epoxy. b) For 20±1 °C cured epoxy.

2.3.6 Fitting of interface constants

The Curve Fitting Toolbox included in the MATLAB (The MathWorks 2011a) was applied for the fitting procedure of the non-linear part of Eqs. (2) and (3). In cases where replicate experiments were performed, the more conservative result was used in the fitting of $t_{\mathrm{II}}(\delta_{\mathrm{II}})$.

Because q governs interface degradation, the fitted material parameters can conventionally be represented as a function of q. Hence, the functions for the critical cohesive stress $t_{\mathrm{II}}^{c}(q)$ and steady friction stress $t_{\mathrm{II}}^{r}(q)$ could be developed by applying the linear least squares method. The decay exponent of Eq. (2), $\alpha \approx$ -5.33 was obtained by calculating an average of the different values of α for each q based on the original test data. By defining a common α and developing Eqs. (4) and (5), the number of parameters is decreased. This unification process, i.e. refitting of the parameters to a single data set, improves the applicability of the interface damage model for engineering purposes. Finally, Eqs. (4) and (5) can be combined with Eq. (2) to give the total

response model $t_{\mathrm{II}}(\delta_{\mathrm{II}},q)$, which is defined as a combination of the terms which are linear in $t_{\mathrm{II}}^{c}(q)$, $t_{\mathrm{II}}^{r}(q)$ and non-linear in α for the selected q. The overall cohesive strength in terms of stress is governed by the scale of $t_{\mathrm{II}}^{c}(q)$.

$$t_{\mathrm{II}}^{c}(q)=0.067q+33.09\,,\quad q\in[50,150] \tag{4}$$

$$t_{\mathrm{II}}^{r}(q)=0.34q+11.47\,,\quad q\in[50,150] \tag{5}$$

Figure 13 shows the corresponding fits calculated from Eq. (2) for $q\in[50,150]$ MPa. These regression fitted curves calculated for each q are based on the unified material parameters, which are presented in Table 6.

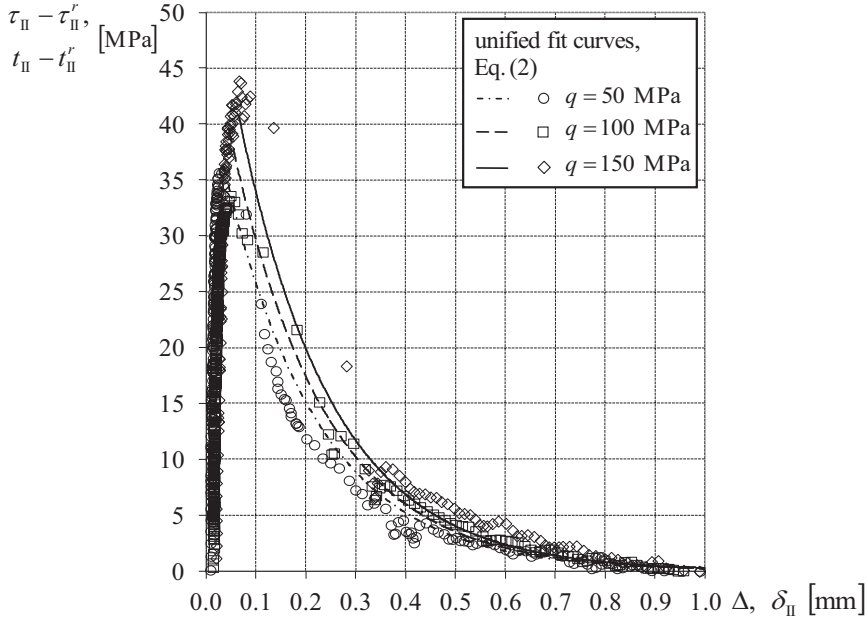

Figure 13. Interfacial decohesion responses of the specimens with the grit blasted contact surface finish involving 65±3 °C cure. The original test data of the conservative results $\tau_{\mathrm{II}}(\Delta)-\tau_{\mathrm{II}}^{r}(\Delta)$ for $q\in[50,150]$ MPa is compared to the fitted exponential decay model $t_{\mathrm{II}}(\delta_{\mathrm{II}},q)-t_{\mathrm{II}}^{r}(q)$, Eq. (2).

To this end, the interface stiffness parameter $\kappa_{II} \in [3 \cdot 10^3, 10^4]$ N/mm^3 can be approximated based on the experimental data presented in Figures 10 and 11. With reference to Figure 12, the numerical values of the critical relative displacements can then be calculated from

$$\delta_{II}^c = \left(t_{II}^c + t_{II}^r\right) / \kappa_{II} . \tag{6}$$

At $\Delta \to 1.0$ mm, $\tau_{II}(\Delta)$ for all reinforced specimens had reached a nearly steady state value. Therefore, the friction coefficient μ_r corresponding to $\tau_{II}(1.0)$ was based on the experimental data, and the values of μ_r were directly calculated from

$$\mu_r(q) = \tau_{II}(1.0) / q . \tag{7}$$

Table 6. Material parameters of the interface damage model as a unified data set for 65±3 °C cured epoxy. The values of μ_r are based on Eq. (7) for each q.

q [MPa]	t_{II}^c [MPa]	α	μ_r
50	36.44	-5.33	0.56
100	39.79	-5.33	0.44
150	43.14	-5.33	0.41

Finally, the continuous curves shown in Figure 14 present the total response model, Eq. (2), the development of which is based on the evaluated experimental degradation responses. The fits based on the original individual data sets are also shown in Figure 14 only as reference.

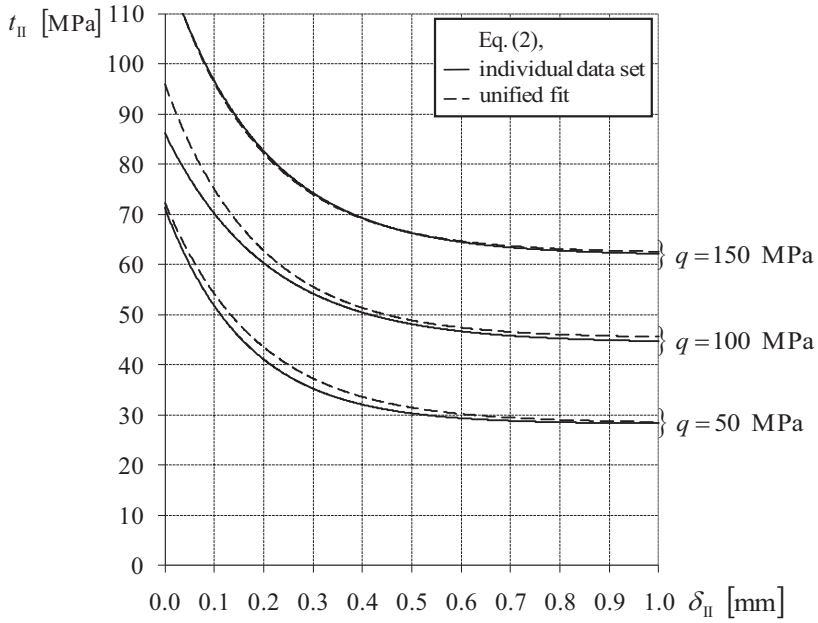

Figure 14. Calculated total response of the specimens with the grit blasted contact surface finish involving 65±3 °C cure. The results based on the unified interface constants are compared to the original individual fits for each q.

Similarly, the non-dimensional shape exponents α, β and the shape scale parameters γ, χ of the total response model, Figure 12b and Eq. (3), were fitted based on the more conservative experimental data plotted in Figure 11. In addition, the functions $t_{II}^{c}(q)$, $t_{II}^{r}(q)$, $\gamma(q)$ and $\chi(q)$ were developed by applying the linear least squares method. The exponents of Eq. (3), α and β were obtained by averaging. The unified material parameters can be calculated from the following equations and are additionally listed in Table 7. The previously presented Eqs. (6) and (7) apply also for this case.

$$t_{II}^{c}(q) = 0.062q + 5.50, \quad q \in [50,200] \tag{8}$$

$$t_{II}^{r}(q) = 0.31q + 9.29, \quad q \in [50,200] \tag{9}$$

$$\gamma(q) = (0.23q + 2.59)/t_{\mathrm{II}}^{c}, \quad q \in [50,200] \tag{10}$$

$$\chi(q) = (-0.23q + 2.78)/t_{\mathrm{II}}^{c}, \quad q \in [50,200] \tag{11}$$

Table 7. Material parameters of the interface damage model as a unified data set for 20±1 °C cured epoxy. The values of μ_r are based on Eq. (7) for each q.

q [MPa]	t_{II}^{c} [MPa]	α	β	γ	χ	μ_r
50	8.58	-4.71	-27.36	1.67	-0.99	0.44
100	11.66	-4.71	-27.36	2.23	-1.69	0.43
150	14.74	-4.71	-27.36	2.56	-2.10	0.40
200	17.82	-4.71	-27.36	2.78	-2.37	0.34

2.4 Post-peak response of non-reinforced interfaces

The combined slip and pure HSS decohesion responses of the specimens without adhesive reinforcement were also experimentally evaluated. This data is necessary in order to assess the adhesive's influence on the shear strength of the interface. The plot presenting $\tau_{\mathrm{II}}(\Delta)$ behaviour for the grit blasted surfaces is shown in Figure 15. The plots for the fine ground and coarse ground specimens are given in Figure 16.

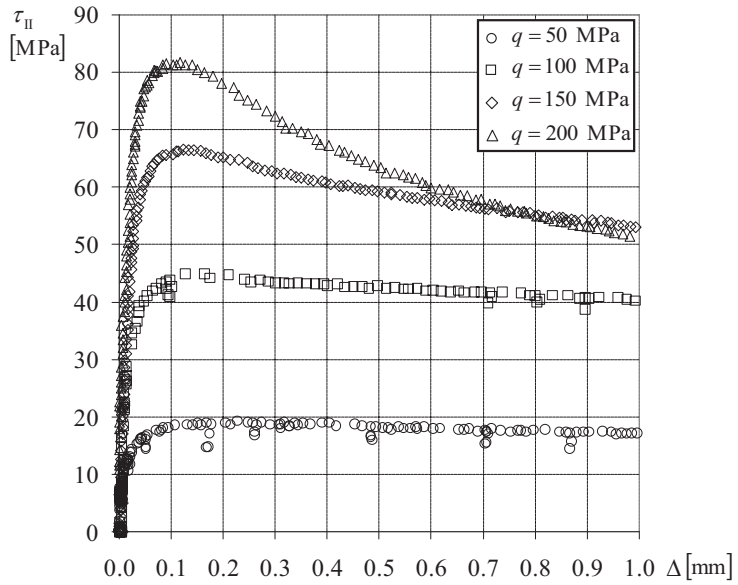

Figure 15. Interfacial degradation responses of the non-reinforced specimens with the grit blasted contact surfaces for each q. The clearly highest interfacial damage (wear of HSS) occurs to the case with the highest clamping load, q = 200 MPa.

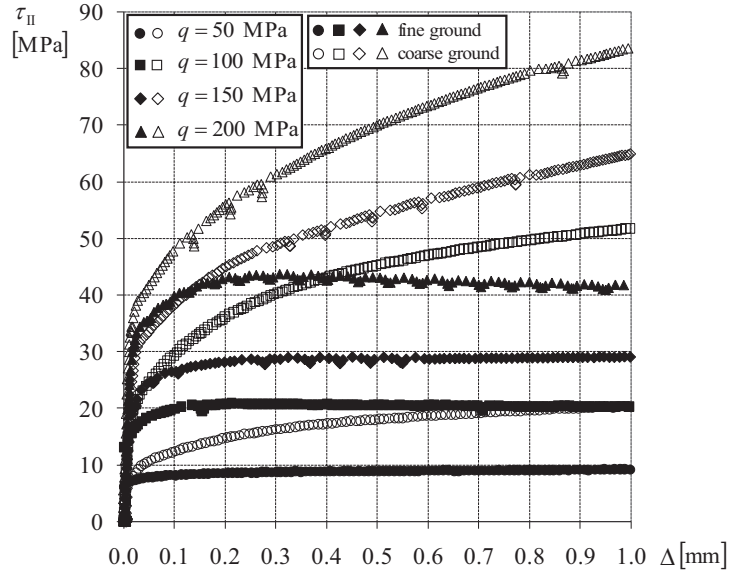

Figure 16. Interfacial slip-response of the non-reinforced specimens with the fine and coarse ground contact surfaces for each q. The fine ground cases most closely resemble the classical Coulomb's friction law after the transient degradation vanishes. For all coarse ground cases, there clearly exists stable interface hardening.

3 Computational damage and slip modelling procedure

In Section 2, the determination of the total shear stress vs. displacement response $\tau_{II}(\Delta)$ of the reinforced specimens was based on the experimentally measured interface degradation. The steady frictional stress of the damaged specimens $\tau_{II}(1.0)$ was subtracted from the total quantity $\tau_{II}(\Delta)$ to obtain the damage response as a result of degradation of the interfaces. Based on this result, the damage evolution equations were parametrically fitted using the least squares method for each case of the pre-stress q.

In the current section, the experimentally characterized decohesion behaviour is exploited in the development of the computational interface damage modelling procedure. Pure shear interfacial damage is studied and an effect of the constant q is included in the interface parameters of the computational damage evolution model. Consequently, the constitutive response of decohesion finite elements is modelled in terms of the traction-separation law with an uncoupled relation between the normal and shear components of the traction vector and separation vector. An exponential damage function involving four material parameters is derived and details of the FE model are described. This damage function was implemented into the ABAQUS environment to govern interface degradation during simulations. Steady dynamic friction is modelled based on the isotropic non-local friction law. Damage is exclusively assumed to occur along the pre-defined decohesion interface. The steady non-local friction and interfacial damage are processed as uncoupled in the performed simulations. The 2D FE test model consists of two plate members and a cohesive interface. To reduce computational effort, only a short segment of the axi-symmetric test surface is modelled. The results of large shear displacement simulations on the test model, $\Delta \in [0,1.0]$ mm, are presented with comparison to the original experimental data.

3.1 Cohesive zone model

The adapted CZM was based on the linear-exponential traction vs. separation response for each of the loading modes (i = I, II, III). This model can be illustrated with the help of Figure 17. The penalty stiffness parameter K_{ii} determines the slope of the line A-B and represents the linear-elastic response area of the reinforced interface for the normal and shear deformation across the interface. The decohesive degradation initiates when the maximum elastic interface traction stress t_i^c is reached at the critical point B. At this inflexion point, the corresponding relative displacement between interfaces δ_i is defined as the critical displacement δ_i^c. As δ_i further increases, t_i varies non-linearly until the full damage corresponding to a zero residual value of t_i at the point C has been accumulated.

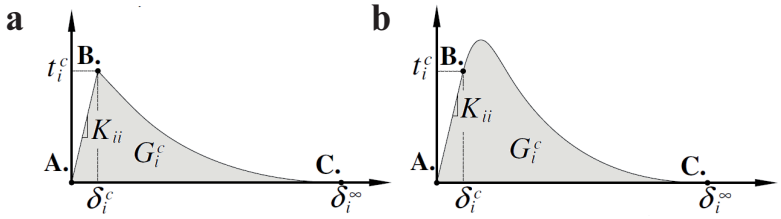

Figure 17. Linear-exponential damage evolution models. The critical fracture energy for each G_i^c mode is defined as an area integral. a) For 65±3 °C cured epoxy. b) For 20±1 °C cured epoxy.

In FEM implementation, the non-zero components of the nominal traction stress vector ***t*** are computed by dividing force components by the initial area at each integration point of the element (ABAQUS Inc 2010). The constitutive thickness of the decohesion interface T_c is appropriately selected equal to unity. Consequently, based on the following definition of linear strains,

$$\varepsilon_i = \delta_i / T_c , \tag{12}$$

the components of the nominal strain vector $\boldsymbol{\varepsilon}$ are equal to the corresponding separations $\boldsymbol{\delta}$ (ABAQUS Inc 2010). The vector $\boldsymbol{t}$ across the reinforced interface is related to $\boldsymbol{\varepsilon}$ by the elastic constitutive matrix $\boldsymbol{K}$. Hence, the linear-elastic behaviour can be written as

$$\begin{Bmatrix} t_1 \\ t_2 \\ t_3 \end{Bmatrix} = \begin{bmatrix} K_{11} & 0 & 0 \\ 0 & K_{22} & 0 \\ 0 & 0 & K_{33} \end{bmatrix} \begin{Bmatrix} \varepsilon_1 \\ \varepsilon_2 \\ \varepsilon_3 \end{Bmatrix}, \tag{13}$$

where the zero terms in off-diagonal of $\boldsymbol{K}$ exist due to selected uncoupled behaviour between the normal and shear components of $\boldsymbol{t}$ and $\boldsymbol{\varepsilon}$. With the equality $\boldsymbol{\varepsilon} = \boldsymbol{\delta}$, the diagonal of $\boldsymbol{K}$ could directly be determined based on the true geometric thickness of the interface T_g (ABAQUS Inc 2010). Camanho et al. (2003) have obtained accurate and well converged computational results for composites by using a value of $K_{ii} = 10^6$ N/mm^3. In contrast to reinforced interfaces, the condition $T_g = 0$ is a result of the normal load q and suggests that the shear plane penalty stiffness parameters $K_{11} \to \infty$ and $K_{22} \to \infty$. However, to obtain converged solutions, the numerical values of $\boldsymbol{K}$ should be selected within the range $K_{ii} \in [10^4, 10^{10}]$ N/mm^3 (Turon et al. 2006). With the numerical stability in mind, a functional selection such as 10^6 N/mm^3 for K_{11} and K_{22} can be adapted.

For three potential loading modes, damage in the cohesive elements is assumed to initiate based on the quadratic interaction function (Dávila and Camanho 2001),

$$\left(\frac{t_1}{t_1^c}\right)^2 + \left(\frac{t_2}{t_2^c}\right)^2 + \left(\frac{\langle t_3 \rangle}{t_3^c}\right)^2 = 1, \tag{14}$$

where the Macaulay brackets $\langle\ \rangle$ in the third component, i.e. the normal component, indicate that exclusively compressive stressing does not allow damage to initiate. This operator is defined by Eq. (15),

$$\langle t_i \rangle = \begin{cases} 0, & t_i < 0 \\ t_i, & t_i \geq 0 \end{cases}. \tag{15}$$

Damage evolution is governed by the damage function $d(\delta_{eff})$, which ranges from zero (undamaged) to one (full damage). The effective displacement δ_{eff}, i.e. the highest value of the mixed-mode relative displacement attained by the interface material, is obtained from the Euclidean norm of $\boldsymbol{\delta}$ (Camanho and Dávila 2002),

$$\delta_{eff} = \|\boldsymbol{\delta}\|, \ \forall \ \langle \delta_3 \rangle . \tag{16}$$

In Eq. (16), the Macaulay brackets in δ_3 indicate that a negative displacement, i.e. penetration due to q at the interface does not affect the numerical value of δ_{eff}. The mode I degradation considerably differs from the mode II damage contribution. For convenience, the condition $\langle \delta_3 \rangle$ is set and the mode I influence due to q is parametrically included in $d(\delta_{eff})$. The degraded stresses are governed by the matrix equation (Camanho and Dávila 2002),

$$\boldsymbol{t} = (\boldsymbol{I} - \boldsymbol{D})\boldsymbol{K}\boldsymbol{\delta}, \tag{17}$$

where $\boldsymbol{D} = d(\delta_{eff})\boldsymbol{I}$ is the damage matrix and $\boldsymbol{I}$ is the identity matrix. The critical fracture energy release rate G_i^c for each mode is defined as the work of separation of the two surfaces (Rice 1968a, 1968b),

$$G_i^c = \int_0^{\delta_i^\infty} t_i(\delta_i) d\delta_i . \tag{18}$$

3.2 Computational decohesion model and damage function

The form of the damage evolution law was suggested based on the form of the experimentally observed damage. In this section, the damage function is derived based on a proposed linear-exponential damage evolution law. The non-linear damage evolution law is formulated as the superposition of two exponential functions. With reference to Figure 17, this damage evolution model is mathematically expressed as,

$$t_i(\delta_i)=\begin{cases} K_{ii}\delta_i, & \delta_i \in [0,\delta_i^c) \\ t_i^c\left[\gamma\exp\left(\alpha\left(\delta_i-\delta_i^c\right)\right)+\chi\exp\left(\beta\left(\delta_i-\delta_i^c\right)\right)\right] & \delta_i \in [\delta_i^c,\delta_i^\infty) \end{cases}, \tag{19}$$

where α, β are the shape exponents and γ, χ are the shape scale parameters, i.e. non-dimensional material constants. Exclusively for the case shown in Figure 17a, γ = 1 and χ = 0. The overall cohesive strength in terms of stress is governed by the scale of t_i^c. The difference of the relative displacements ($\delta_i-\delta_i^c$) in Eq. (19) exists because the non-linear part of the damage evolution law is defined to be valid for the displacement range $\delta_i \in [\delta_i^c, \delta_i^\infty)$. From the constitutive relation, Eq. (17), t_i (δ_i) can be defined,

$$t_i(\delta_i)=K_{ii}\delta_i(1-d). \tag{20}$$

The equation of the interface stress degradation can be expanded by substituting Eq. (19) with an identity $t_i^c = K_{ii}\delta_i^c$ into Eq. (20) as follows,

$$K_{ii}\delta_i(1-d)=\gamma K_{ii}\delta_i^c\exp\left(\alpha\left(\delta_i-\delta_i^c\right)\right)+\chi K_{ii}\delta_i^c\exp\left(\beta\left(\delta_i-\delta_i^c\right)\right),\ \ \delta_i^c>0,\ \ \delta_i\in\left[\delta_i^c,\delta_i^\infty\right). \tag{21}$$

To develop the damage evolution function $d(\delta_{eff})$, the effective displacement δ_{eff} is considered. Firstly, from Eqs. (19) and (20) we obtain a trivial solution $d(\delta_{eff})$ = 0 for the range $\delta_{eff} \in [0, \delta_{eff}^c)$. Secondly, Eq. (21) can further be modified and simplified for the range $\delta_{eff} \in [\delta_{eff}^c, \delta_{eff}^\infty)$ to the form,

$$\delta_{eff}(1-d)=\gamma\delta_{eff}^c\exp\left(\alpha\left(\delta_{eff}-\delta_{eff}^c\right)\right)+\chi\delta_{eff}^c\exp\left(\beta\left(\delta_{eff}-\delta_{eff}^c\right)\right),\ \ \delta_{eff}^c>0,\ \ \delta_{eff}\in\left[\delta_{eff}^c,\delta_i^\infty\right). \tag{22}$$

Finally, $d(\delta_{eff})$ corresponding to its damage evolution law is completed by solving Eq. (22) for $d(\delta_{eff})$,

$$d(\delta_{eff}) = \begin{cases} 0, & \delta_{eff} \in [0, \delta_{eff}^{c}) \\ \delta_{eff}^{-1}\left[\delta_{eff} - \gamma\delta_{eff}^{c}\exp\left(\alpha\left(\delta_{eff} - \delta_{eff}^{c}\right)\right) - \chi\delta_{eff}^{c}\exp\left(\beta\left(\delta_{eff} - \delta_{eff}^{c}\right)\right)\right], & \delta_{eff} \in [\delta_{eff}^{c}, \delta_{eff}^{\infty}) \end{cases},$$
$$d \in [0,1]. \tag{23}$$

Based on Eq. (16), the maximum attained value of δ_{eff} is used in Eq. (23) to track the accumulation of the damage, i.e. to ensure that the damage process in non-recoverable.

3.3 Frictional contact interaction model

The contact pairs at the interfaces were modelled by exploiting a penalty contact algorithm with the ABAQUS/Explicit. See e.g. Zhong (1993) for details concerning a theory and formulation of the penalty contact method. The finite sliding tracking approach was chosen, in which the contact is monitored along the entire master surface (ABAQUS Inc 2010). In the normal direction, the hard contact model (ABAQUS Inc 2010) was selected. This model assumes that the contacting surfaces can transmit contact pressure only when the nodes of the slave surface are in contact with the master surface. For reinforced frictional interfaces involving both shear and compressive normal loads, the selected material property $K_{33} \to 0$ allows the use of non-local friction models without interference.

Isotropic non-local friction was modelled along the contacting surfaces based on the static-kinetic formulation (ABAQUS Inc 2010). This friction law is based on the assumption that no relative sliding can occur if the equivalent friction stress τ_{eq} computed from

$$\tau_{eq} = \sqrt{\tau_1^2 + \tau_2^2} \tag{24}$$

is less than the corresponding critical shear stress,

$$\tau_{cr} = \mu_r |\sigma_3|, \tag{25}$$

where σ_3 is the initial normal stress to slip and μ_r is the friction coefficient. In Eq. (24) τ_1 and τ_2 are the computed shear stresses at the contact surfaces. Correspondingly, for the adapted 2D model shown in Section 3.4, the non-slip state is valid for the condition $\tau_1 < \tau_{cr}$, where $\tau_{cr} = \mu_r |\sigma_2|$.

An influence of the rough surfaces on the tangential stiffness κ_{II} was taken into account in the adapted frictional model to improve the correlation with the test data. The tangential stiffness of the contact interface κ_{II} was specified to determine the slope of the shear stress vs. elastic slip relationship, i.e. sticking frictional behaviour. Based on trial simulations and the test data represented in Section 2.3.4, the value of κ_{II} was selected to 10^4 N/mm^3 for all simulations on the 2D test model. For rough surfaces, a non-linear dependence between κ_{II} and q could be expected (Oden and Martins 1985). In this study, however, the constant κ_{II} was found to result to a good correlation with the experimental results shown in Section 2.3.4 for all values of q. This insensitivity can be explained by a relatively small range of the studied pre-load, i.e. $q \in [50,200]$ MPa.

3.4 Finite element based simulation – 2D test model

The 2D FE model involving the two plate members and cohesive interface is shown in Figure 18. The bottom plate was modelled slightly longer to allow for sufficient displacement $\tilde{\Delta}$ of the upper plate and to allow more uniform distribution of the stress fields. Only a short section of the joint was modelled to reduce computational cost. Thus, the resulting FE model corresponded to a section equal to about 2 % of the circular test specimen area which is shown in Figure 1. For the FE model setup, four node quadrilateral plane stress CPS4R continuum elements and COH2D4 cohesive elements were used with the ABAQUS/Explicit. The cohesive elements with two integration points had sharing nodes with the neighbouring continuum elements. A geometric thickness of zero, T_g = 0, was used for the cohesive layer of elements. The bottom nodes of the lower plate were constrained in both directions.

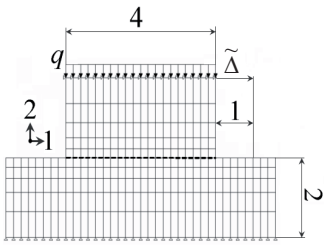

Figure 18. FE model of the reinforced connection, including two plate members. The mesh size is 0.2 x 0.2 mm at the interface. The interface composed of the zero thickness cohesive elements is marked with the dashed line. The horizontal displacement, $\tilde{\Delta} \rightarrow 1.0$ mm, due to the transverse velocity boundary condition applies along all nodes of the top surface, which is simultaneously affected by the normal pressure q.

Failure simulations were performed in two steps. Firstly, a tightening operation was simulated by imposing the desired constant q acting on the top of the upper plate member in the negative 2 direction. Secondly, a constant horizontal translational velocity boundary condition was imposed to induce shear stress. This translation was applied along the top surface of the upper plate and was in the positive 1 direction. The translation was slow enough for the resulting solution to become quasi-static, and dynamic effects, such as oscillatory effects due to inertial forces, were insignificant. The rate of 0.5 m/s was used for the simulated clamping operation, and the constant translation velocity was 0.05 m/s. Note that the damage evolution equations do not contain any time-dependent terms, thus the rate is selected only to obtain a good numerical solution.

The test specimens were manufactured from steel, so typical values for the Young's modulus 210 GPa, Poisson's ratio 0.3 and density $7.8 \cdot 10^3$ kg/m^3 were used for the FE model. The material parameters for both the friction model and CZM were derived from the experimental data and are described in Section 2.3.4. The fine mesh size 0.2 x 0.2 mm at the contact interface was modelled to ensure a convergence of stresses. This selection was based on previous work by Turon et al. (2006), who comment on the mesh sensitivity of CZM and the influence of the cohesive layer stiffness K_{ii} on the computational results. Considerably coarser mesh size has been found to result in good

engineering accuracy and thus improved computational efficiency in debonding simulations (Turon et al. 2006).

The FE models of this study involved processes that change over short time intervals, i.e. demonstrate progressive degradation of the reinforced interconnection or interfacial slip. In such cases, convergence problems with the implicit Newton-Raphson solver could occur and thus increase the computational cost (Bathe 1996). For explicit solution methods, the state at the end of each increment is based on the computed displacements and their first and second derivatives from the previous increment (Bathe 1996; ABAQUS Inc 2010). Advantages of explicit methods over implicit methods are that each time increment is inexpensive and complex contact problems can be solved more promptly (ABAQUS Inc 2010). Therefore, the FE problems were solved using the central difference method based explicit integration with the ABAQUS/Explicit.

3.5 Computed shear damage responses – 2D test problem

Figure 19 shows the combined slip and decohesion response of reinforced grit blasted specimens in the range of resulted relative displacements $\Delta \in [0,1.0]$ mm. The results corresponding to adhesive cured at room temperature are presented. The computed FE solution of the total interface shear stress $\tau_{II}(\Delta)$ is shown with the experimental data. The reference result for each case of *q* is the more conservative one of the two identical experiments shown in Figure 11. Here, the conservative result indicates the data series which attained the lower peak value of $\tau_{II}(\Delta)$. The conservative results were adapted as references for the fitting of the damage evolution model parameters in Section 2.3.6. The continuous dashed curves represent the corresponding simulation results based on the unified material parameters, i.e. the single data sets, given in Table 7. The continuous reference curves present the corresponding computational results based on the original individual fits. As $\Delta \to 1.0$, the shear load carrying capacities approach steady state, corresponding to full interface damage, $d(\delta_{eff}) \to 1.0$. In the current example, $\Delta \approx \widetilde{\Delta}$.

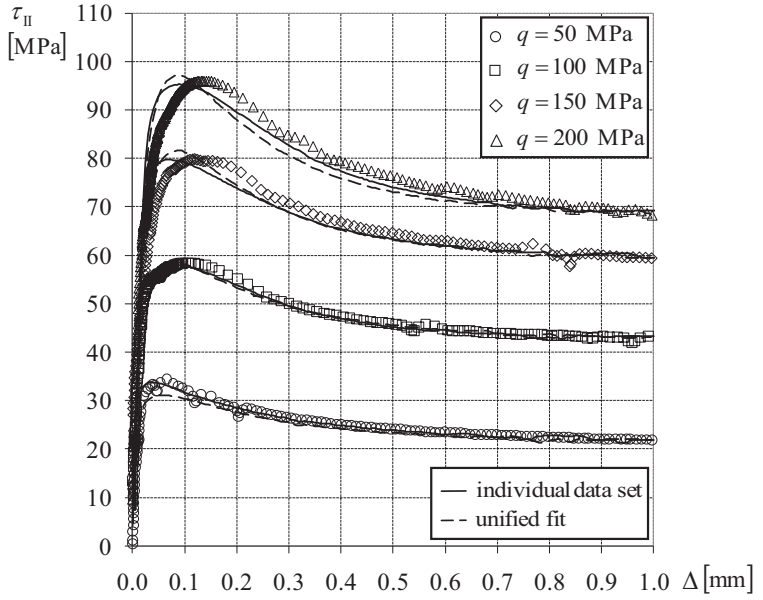

Figure 19. Continuous curves present the FE solution of the combined slip and interface damage responses for each q. The numerical results are compared to the respective more conservative original experimental data.

4 Interfacial fracture energy release rate

The fracture resistance curve, *R*-curve, has been developed to describe energy release rate as a crack advances in a ductile or semi-ductile material. In this work the damage process is associated with relative displacement of the interfaces so an analogous concept, the *G*-curve is developed. The *G*-curve represents the failure energy release rate per unit area of the cohesive zone as a function of displacement.

In this section, the *G*-curves for the grit blasted specimens cured at room temperature are produced. In addition, the G_{eff}-curves for both the heat-cured grit blasted specimens and fine ground specimens cured at room temperature are produced to represent the development of the mode II energy release rate G_{II} vs. relative displacement Δ. This classification is based on the experimentally observed shear fracture behaviour strongly affected by the cure temperature of the epoxy adhesive used.

4.1 *G*-curves of adhesive reinforced interfaces

For the characterized traction stress t_i vs. relative displacement δ_i relationship, the fracture energy release rate G_i is obtained by integrating Eq. (19) with respect to δ_i within $\delta_i > 0$. The resulting total potential functional for is then,

$$G_i\left(\delta_i\right) = t_i^c \delta_i^{c^{-1}} \int_0^{\delta_i^c} \delta_i d\delta_i + t_i^c \int_{\delta_i^c}^{\delta_i} \left[\gamma \exp\left(\alpha\left(\delta_i - \delta_i^c\right)\right) + \chi \exp\left(\beta\left(\delta_i - \delta_i^c\right)\right)\right] d\delta_i \,, \quad \delta_i^c > 0 \,,$$
$$\delta_i \in \left[\delta_i^c, \delta_i^\infty\right) \,. \tag{26}$$

From Eq. (26), one can obtain the equation to be used for computing the critical fracture energy release rate,

$$G_i^c = t_i^c \left\{ 2^{-1} \delta_i^c + \gamma \alpha^{-1} \left[\exp\left(\alpha\left(\delta_i^\infty - \delta_i^c\right)\right) - 1\right] + \chi \beta^{-1} \left[\exp\left(\beta\left(\delta_i^\infty - \delta_i^c\right)\right) - 1\right] \right\} \,, \quad \delta_i^c > 0 \,. \tag{27}$$

In Eq. (27), the first term inside the braces gives the contribution of the linear portion of the damage evolution law to G_i^c. The second and third terms define the contribution of the non-linear portion of the damage evolution law to G_i^c, respectively. The linear part of Eq. (27) approaches zero for cases involving high interface stiffness.

The computed shear energy release rate G_{II} vs. Δ, i.e. *G*-curves of the grit blasted interfaces cured at room temperature, are shown in Figure 20. As $\Delta \to 1.0$ mm, G_{II} has approximately reached to G_{II}^c. To validate the goodness of the fitted non-dimensional shape parameters (Table 7), the corresponding *G*-curves were also computed by directly numerically integrating the original experimental data with respect to Δ.

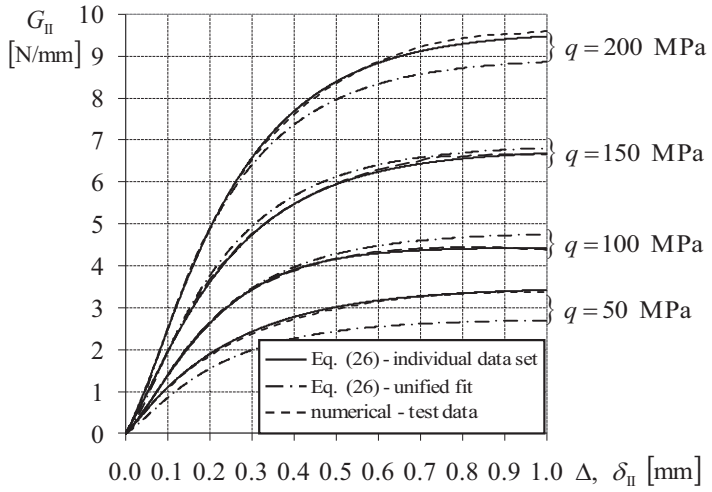

Figure 20. *G*-curves of the grit blasted interfaces cured at room temperature for one week. The results computed by Eq. (26) are shown with comparison to the corresponding curves, which were integrated based on the more conservative experimental result data.

4.2 Effective *G*-curves of adhesive reinforced interfaces

The shear energy release rate G_{II} vs. Δ, i.e. G_{eff}-curves of the reinforced interfaces, are shown in Figure 21 for the grit blasted surface finish and in Figure 22 for the fine ground finish. In Figure 22, the results corresponding to adhesive cured at room

temperature are shown. These G_{eff}-curves were numerically integrated based on the original test data points. For all cases, G_{II} has reached approximately constant values at Δ = 1.0 mm. This is defined as G_{II}^{c}. With reference to CZMs shown in Figure 17 involving G_{II}^{c} defined by Eq. (28), the G_{eff}-curves exclusively include damage dissipation of the reinforced interface, and the contribution of steady frictional dissipation is excluded (Oinonen and Marquis 2011a, 2011b). The cases involving the predominantly brittle or unstable decohesion fracture were considered as non-relevant sources, and the respective G_{eff}-curves could not be developed. In contrast to the G-curves shown in Figure 20, the G_{eff}-curves in Figures 21 and 22 are presented as data points to emphasize discontinuities due to the brittle fracture intervals.

$$G_{\mathrm{II}}^{c} = \int_{0}^{1.0} \left[\tau_{\mathrm{II}}(\Delta) - \tau_{\mathrm{II}}(1.0) \right] d\Delta \tag{28}$$

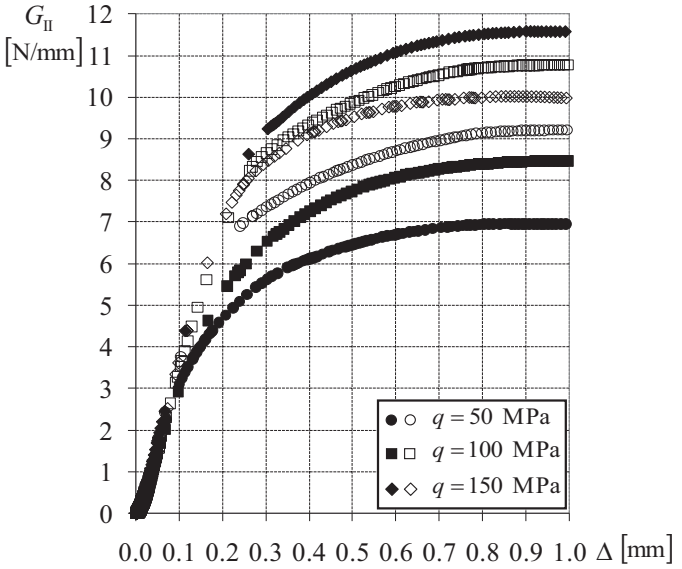

Figure 21. G_{eff}-curves of the adhesive reinforced interfaces with the grit blasted surface finish. The filled markers correspond to the conservative result obtained from two identical tests. Epoxy adhesive was cured at 65±3 °C.

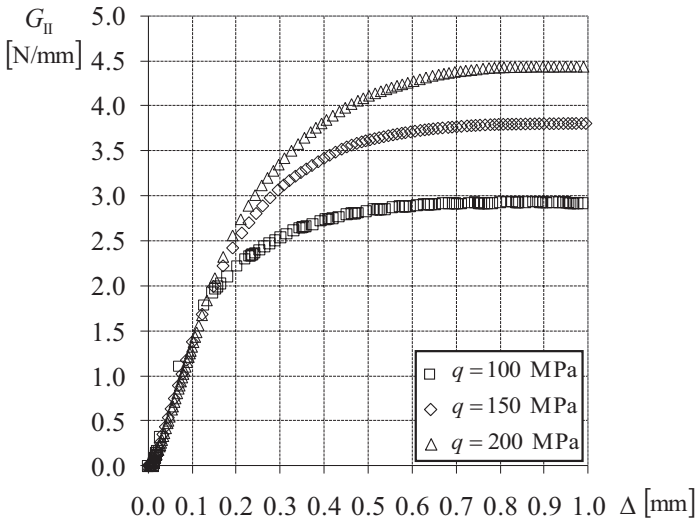

Figure 22. G_{eff}-curves of the reinforced interfaces with the fine ground surface finish. Epoxy adhesive was cured at 20±2 °C.

5 Testing and simulation of full-scale adhesive reinforced bolted lap-joints

The applied research part of this thesis is concerned with assessment of the total shear load carrying capacity of full-scale double lap-connections. A double lap-joint resembles the geometry of many bolted joints applicable in structural engineering. Moreover, the connection is cost-effective and relatively simple to manufacture. The good structural performance of this type of joint is a result of both the symmetric direct load path and increased slip load capacity due to double frictional planes. The symmetric load path is also very favourable for laboratory testing. However, the true stress distribution at the lap-interfaces, which are simultaneously subject to the direct shear and clamping loads is, characteristically, non-uniform and complex.

Quasi-static testing on the bolted full-scale specimens was performed. The connections involved epoxy adhesive reinforced HSS interfaces tightened to a pre-defined tension values which was measured using instrumented HS bolts. The expected distribution of normal pressure in the contact region in the vicinity of the bolt was determined using FEA. The experimental programme included two parallel fasteners and three fasteners in a series (row). Joints both with and without adhesive reinforcement were tested. Two alternate bolt pre-load values were used. The maximum attained shear loads are reported and comparisons to the results based on the identical non-bonded specimens are made.

The corresponding 3D interface damage simulations on the reinforced connections were computed using FEM. The numerical values of the maximum shear loads are summarized with comparison to the experimental results. In addition, the attained direct shear load vs. relative displacement curves are produced based on the numerical results.

5.1 Experiments on the double lap-connections

The full-scale test specimens were fabricated from the same material as the napkin ring specimens of this study, i.e. HSS sheet with yield strength 960 MPa and plate thickness 8 mm. The schematic of the double lap-connections with the key details and features is shown in Figure 23. The testing matrix and specimen identifications (ID) are listed in Table 8. Two different fastener layouts were investigated, i.e. the parallel and row connections with the z number of instrumented HS bolts. For the reinforced specimens, two replicate tests were performed with both values of the pre-specified clamping load P_f. In total, the results of twelve experiments are reported.

Table 8. Testing matrix.

Specimen ID	Interface type	z	Layout	P_f [kN]
2N35-1	non-bonded	2	parallel	35
2N50-1	non-bonded	2	parallel	50
3N35-1	non-bonded	3	row	35
3N50-1	non-bonded	3	row	50
2R35-1, 2R35-2	reinforced	2	parallel	35
2R50-1, 2R50-2	reinforced	2	parallel	50
3R35-1, 3R35-2	reinforced	3	row	35
3R50-1, 3R50-2	reinforced	3	row	50

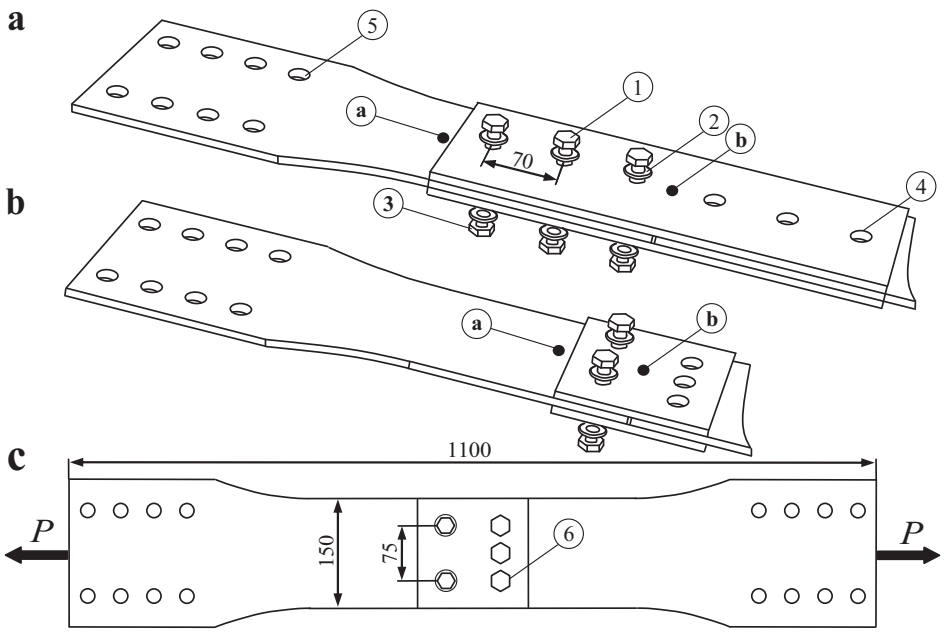

Figure 23. Schematic of the full-scale double lap-connection specimens. The key components and features are: (1) instrumented HS bolts (2 or 3 per specimen), (2) HS washer, (3) nut, (4) oversized bolt through holes of the non-slip half, (5) bolt through holes of the grip end, and (6) oversized bolts and nuts used to ensure non-slip connection. Measurement of the total relative displacement $\tilde{\Delta}$ was performed between the shown location points (**a**) and (**b**). a) Row (series) connection with three fasteners. b) Two single fasteners in parallel. c) Assembled specimen with the main dimensions and direct loads *P*.

5.1.1 Preparation, assembly and cure of the test specimens

The annular contact surfaces of the specimens with the outer limit radiuses r_a were treated by grit blasting using aluminium oxide. The blasting process and resulting interface finish resembled the napkin ring specimens reported in Section 2.1 of this thesis. Figure 24 illustrates both the definition of r_a = 20±0.8 and the radius of the machined holes r_b = 7.25±0.03 mm. The selection of r_a was based on desired closed interface, which was approximated from reference FEA reported in Section 5.2.1. The

surfaces outside of r_a were abraded by hand using a sand paper with the medium grit size, i.e. P60. The result of this treatment can be observed from Figure 24b.

During the assembly process of the reinforced specimens, the epoxy adhesive DP760 (3M United Kingdom PLC 2001) was applied to the annular contact surfaces of the plate members. A template with the hole and putty knife were used for a controlled adhesive application process. The instrumented HS bolts (M12) were centred with the machined holes, and immediately tightened to the pre-specified P_f. Two machined pins were used for centring the holes. The resulted flow of the uncured adhesive due to P_f can be observed from Figure B1 in Appendix B. Two HS washers with the outer radius r_w = 11.9 mm and thickness 2.4 mm were used in conjunction with the instrumented HS bolts. The bolt-head thickness was 7.2 mm.

Similar to the napkin ring specimens of this study, the heat cure of adhesive was performed at 65±3 °C for two hours; the heat-up period from 20 to 65 °C was 2½ hours. The HS bolts remained tight during the entire curing process and subsequent testing process.

5.1.2 Testing procedure

The experiments were performed on a 400 kN static capacity servo controlled loading frame. All specimens were loaded incrementally under displacement control with the nominal rate of 0.027 mm/s, measured from the piston of the hydraulic cylinder of the testing machine. The force and local joint displacements were recorded until the complete failure of the reinforced connection interface, i.e. after the sudden noticeable slip occurred. During testing, the temperature was maintained at 20±1 °C. The assembled and instrumented specimen is shown in Figure B2 in Appendix B.

5.1.3 Fracture behaviour and mechanism

The total response $P(\widetilde{\Delta})$ consists of the local and global responses, i.e. combined decohesive failure and slip at the contact and elastic elongation of the plate members. For all adhesive reinforced specimens listed in Table 8, a sudden fracture occurred after attaining the maximum shear load carrying capacity P_p. Similar to the experiments on

the napkin ring specimens, the non-bonded full-scale lap-connections showed smooth and ductile degradation behaviour, i.e. wear of the abraded HSS. This observation is based on the P/z ($\widetilde{\Delta}$) responses reported in Figures 29-31, Section 5.4.

Figure 24a shows the fully damaged contact surface for P_f = 50 kN and $\widetilde{\Delta} \rightarrow 1.25$ mm. Based on Figure 24a, the interfacial fracture mechanism was due to cohesive failure at the grit blasted interface area limited by $r \in (r_b, r_a)$. In contrast, the abraded smoother surface, $r > r_a$, shows the predominantly adhesive failure. More details of the observable fracture mechanisms are reported in Appendix B, where the damaged contact surfaces of the adhesive reinforced row connection are presented in Figure B1.

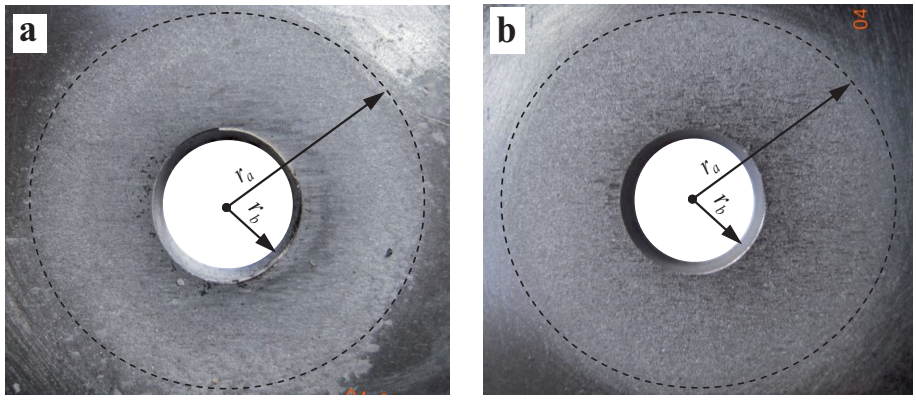

Figure 24. Damaged contact surfaces of the parallel connection for the clamping load P_f = 50 kN and relative displacement $\widetilde{\Delta} \rightarrow 1.25$ mm. The annular interfaces are determined by the limit radiuses, r_a = 20±0.8 and r_b = 7.25±0.03 mm, respectively. a) Adhesive reinforced test specimen. b) Non-bonded case.

5.2 Finite element modelling

In order to more accurately simulate physical behaviour of the bolted structural connection (Kim et al. 2007), a solid bolt model was chosen as the approach in this study. In addition, all FEA involved the Lagrangian formulation (Belytschko et al. 2001; ABAQUS Inc 2010). Hence, the non-linear effects of large deformations and displacements were taken into account. The experimentally determined CZM was

exploited in the FE based simulation procedure. The steady non-local friction was also incorporated into the interaction between the contacting elements.

5.2.1 Determination of the annular interface area

Determination of the outer radius of the contact interface r_a was based on the reference FE model, which was solved using ABAQUS/Standard. Additionally, alternative and more direct methods to determine r_a are studied for comparison. This FE solution, from which r_a is determined, is shown in Figure 25. Figure 25a shows the profile of the interface following tightening with the deformations scaled by a factor 100. Note, that the involved bolt and washers are hidden to enable a more clear presentation. Opening of the interface due to P_f determines the true contacting interface area (Gould and Mikic 1972).

The absolute value of the normal pressure at the contact $|\sigma_3|(r)$ for P_f = 50 kN is plotted in Figure 26. The form of the corresponding solution of r_a as $\sigma_3(r) \to 0$ with P_f = 35 is nearly identical and not here presented. The normalized quantity of $\sigma_3(r)$ is plotted in Figure 27. Comparisons with the classical engineering approximation (Rötscher 1927; Yoshimi 2008) and the analytical solution derived by Chandrashekhara and Muthanna (1979) are also presented. Only FEM takes geometric non-linearity into account. The solution of r_a as $\sigma_3(r) \to 0$ based on the presented reference solutions is independent on P_f for all $P_f \in (0, \infty)$. Obviously, the FE solution requires the highest computational efforts.

The straightforward method to obtain r_a suggested by Rötscher (1927) is based on the assumption that P_f distributes its influence exclusively within the truncated cone involving a vertical half angle of 45° with the axis of the bolt.

The analytical solution derived by Chandrashekhara and Muthanna (1979) is based on the classical theory of elasticity (Love 1944), where the body of revolution under an axial symmetry of the loading is considered. The load due to a bolt is approximated as the constant pressure *q*, which affects on the annular area of the plate member. In order to define the annular area, the constants for the inner radius r_b = 7.25 and outer radius r_w = 11.9 mm, were adapted for the result plotted in Figure 27. Hence, *q* is assumed to uniformly affect through the washer and plate contact.

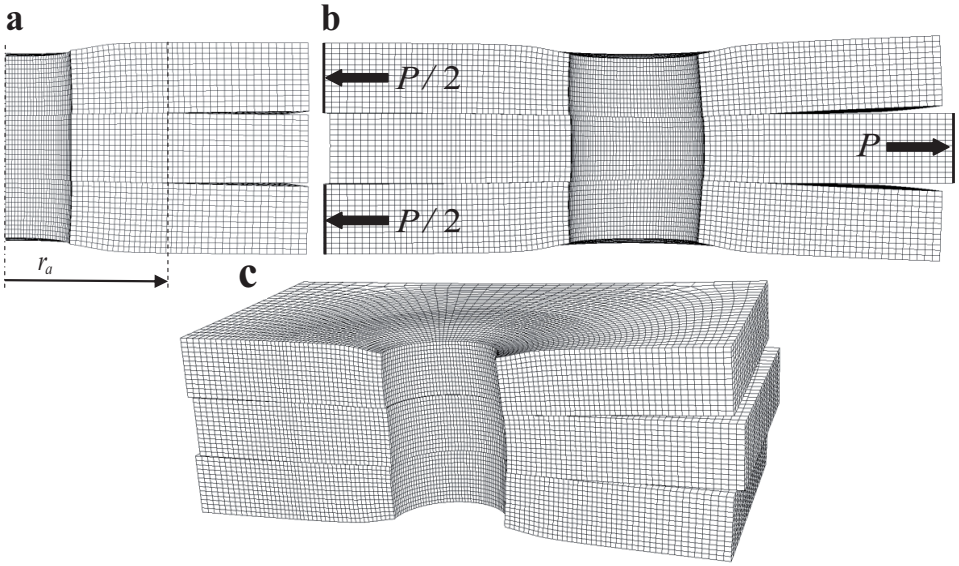

Figure 25. FE solution of the clamped joint with the deformations scaled by a factor 100. The model was solved with the clamping load P_f = 50 kN and friction coefficient μ = 0.4. The similar bolt with washer shown in Figure 28 was used to generate P_f. Here, the bolt and washers are hidden for more illustrative presentation. The mesh size is 0.6 x 0.6 mm in the vicinity of the interface. a) Symmetric opening of the interface occurs exclusively due to P_f. b) Opening of the interface can be observed at the right side due to the combined P_f and *P*. c) General 3D view of the FE solution shown in b).

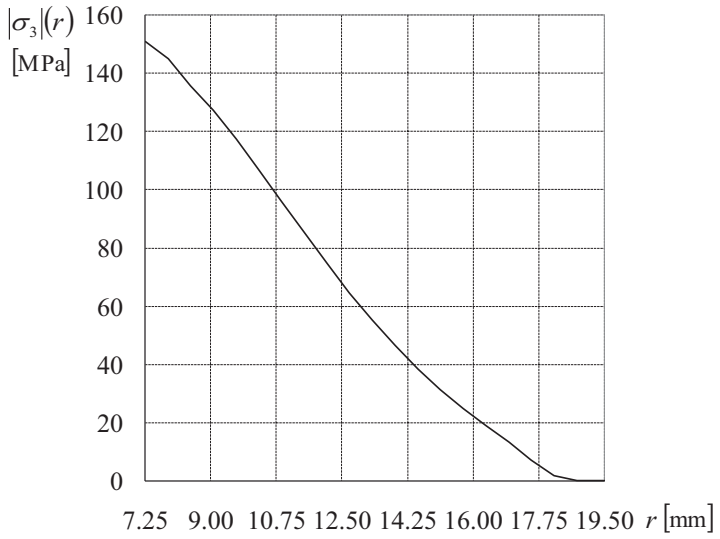

Figure 26. Absolute value of the normal pressure $|\sigma_3|(r)$ at the contact computed using the FE model shown in Figure 25a. The clamping load P_f = 50 kN.

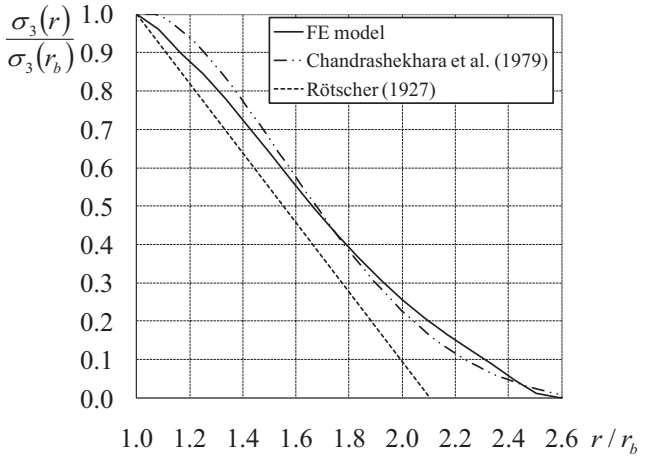

Figure 27. Normalized normal pressure at the contact computed using the FE model shown in Figure 25a. The approximation (Rötscher 1927) and the analytical solution derived by Chandrashekhara and Muthanna (1979) are shown for comparison purposes.

5.2.2 Decohesion and frictional interaction models

With reference to Figure 17a, the adapted CZM involved the damage evolution model of the exponential type. For convenience, the constant pre-stress independent portion of the interfacial shear load carrying capacity B was used as a weight parameter, i.e. the critical shear stress t_{II}^{c} of the damage evolution model. Hence from Table 4, B = 44.56 MPa was adapted as the average value of t_{II}^{c} = 44.56 MPa. This simplification is justified due to the varying and non-uniform $\sigma_3(r)$ distribution at the decohesion interfaces during the progressive damage.

Non-local friction between all contacting surfaces was modelled based on the classical Coulomb's law. In contrast to Section 3.3, the tangential stiffness of the contact interface was specified to $\kappa_{\mathrm{II}} = \infty$, i.e. micro-slipping was not allowed. The friction coefficient corresponding to the steady friction stress was dependent on the local contact pressure at the interface, i.e. $\mu_r(\sigma_3)$. The data points from Table 6 were exploited to determine $\mu_r(q)$. The linear interpolation between the experimental data points $\mu_r(q)$ was applied.

5.2.3 Finite element model and simulation process

The FE model of the single fastener in parallel connection involving the plate members, annular decohesion interface and bolt with the washer is shown in Figure 28. Symmetry of the specimen was exploited in the modelling to reduce computational cost. The resulting FE model corresponded then to a quarter of a single fastener and the surrounding plate material environment of the test specimen shown in Figure 23b. For the series (row) connection shown in Figure 23a, the corresponding FE model involved a row pattern of three identical meshes shown in Figure 28. Decohesion elements (Camanho and Dávila 2002; ABAQUS Inc 2010) with zero thickness were placed at the annular bonded contact interface areas bounded by the radiuses r_a = 20 and r_b = 7.25 mm. Eight node linear brick C3D8R solid elements and COH3D8 cohesive elements were used with the ABAQUS/Explicit. The cohesive elements with four integration points had sharing nodes with the neighbouring solid continuum elements.

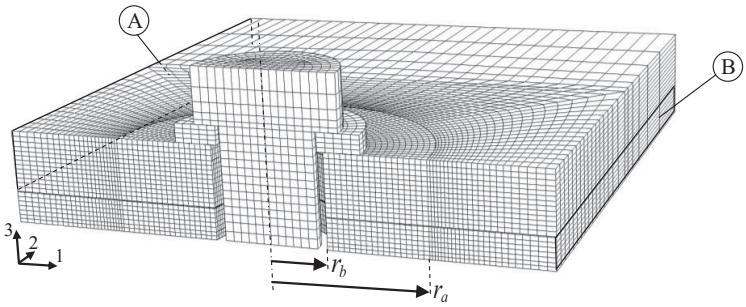

Figure 28. FE model of the single fastener joint. Symmetry was exploited in the modelling. For the parallel connection with two bolts, the model shown here corresponds to ⅛ of the respective environment of the real specimen. The mesh size is 0.6 x 0.6 mm in the vicinity of the decohesion interface.

The failure simulations computed using the FE model shown in Figure 28 were performed in two steps. Firstly, the connection was tightened to a pre-specified P_f by constant pressure acting in the negative direction 3 on the fastener's symmetry plane 1-2, see Figure 28. In the next step, horizontal translational velocity loading condition was applied to generate the desired shear load. This loading was applied along the surface B, to the positive direction 1. The surface A was correspondingly constrained in direction 1.

The kinematic conditions were applied at a slow rate to minimize oscillatory effects due to inertial forces. In all simulations, a time value $5 \cdot 10^{-3}$ s was used in smooth clamping, and a constant rate of 50 mm/s was used to apply the shear load. Additional simulations showed that lower rates did not noticeably influence the final results. Recall from Section 3.4, that the rate is selected only to obtain a good numerical solution with the ABAQUS/Explicit. Both the damage evolution and friction interaction laws do not contain any time-dependent terms.

5.3 Maximum shear load carrying capacity

The measured and simulated maximum values of the attained shear loads P_p are summarized in Table 9. The computed results for the row connection with six fasteners, 6R50-1 and 6R35-1, are provided as an additional interest. In addition, P_p of the identical non-bonded double lap-joints were measured and thus the friction coefficient corresponding to the peak load μ_p can be calculated from,

$$\mu_p = \frac{P_p}{2zP_f}. \tag{29}$$

Table 9. Measured and simulated peak shear loads P_p [kN]. For the non-bonded specimens, the friction coefficients corresponding to the peak load μ_p are listed.

Specimen ID	P_p test	P_p simulation	P_p / z test	P_p / z simulation	μ_p
2N35-1	63.8		31.9		0.46
2N50-1	96.8		48.4		0.48
3N35-1	110.5		36.8		0.53
3N50-1	167.6		55.9		0.56
2R35-1	296.8	240.2	148.4	120.1	
2R35-2	300.7		150.4		
2R50-1	273.4	260.4	136.7	130.2	
2R50-2	287.9		144.0		
3R35-1	330.9	322.4	110.3	107.5	
3R35-2	342.5		114.2		
3R50-1	361.5	353.9	120.5	118.0	
3R50-2	367.5		122.5		
6R35-1		510.5		85.1	
6R50-1		564.1		94.0	

5.4 Total shear load vs. displacement responses

For full-scale lap-joints, $\widetilde{\Delta}$ corresponds to the measured or computed relative displacement between the reference points (**a**) and (**b**), see from Figure 23 and Figure B2, Appendix B. The resulting measured and simulated responses for the parallel connection are shown in Figure 29 and for the row layout in Figure 30, respectively. For adhesive reinforced specimens, exclusively the more conservative, i.e. lower P_p, data is shown from cases where replicate tests were performed. In Figure 31, the experimental results of the identical non-bonded specimens are plotted for $\widetilde{\Delta} \rightarrow 1.0$ mm. In Figures 29-31, the averaged total responses corresponding to the contribution of one fastener are presented.

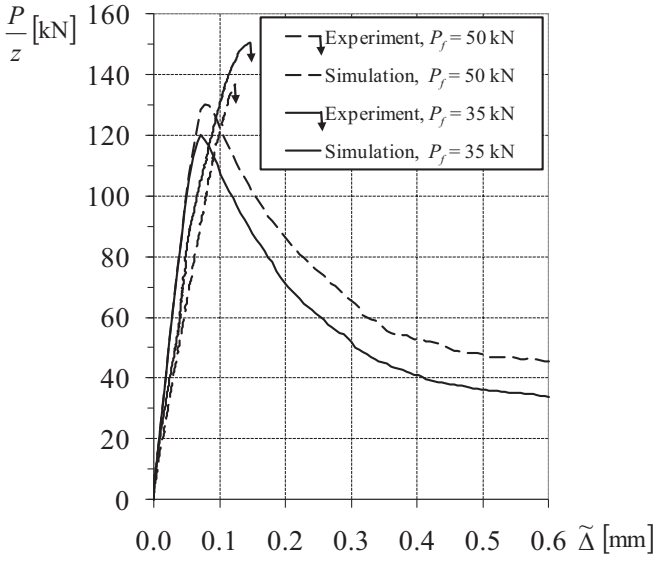

Figure 29. Averaged total response corresponding to the contribution of one fastener. The experimental results of the adhesive reinforced connection for the parallel pattern, Figure 23b, are shown with comparison to the numerical results. For scaling, z = 2 has been used.

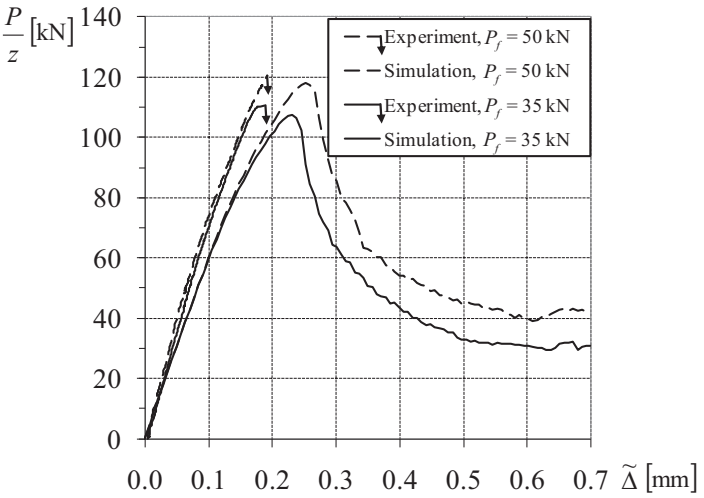

Figure 30. Averaged total response corresponding to the contribution of one fastener. The experimental results of the reinforced connection for the row layout, Figure 23a, are shown with comparison to the numerical results. For scaling, $z = 3$ has been used.

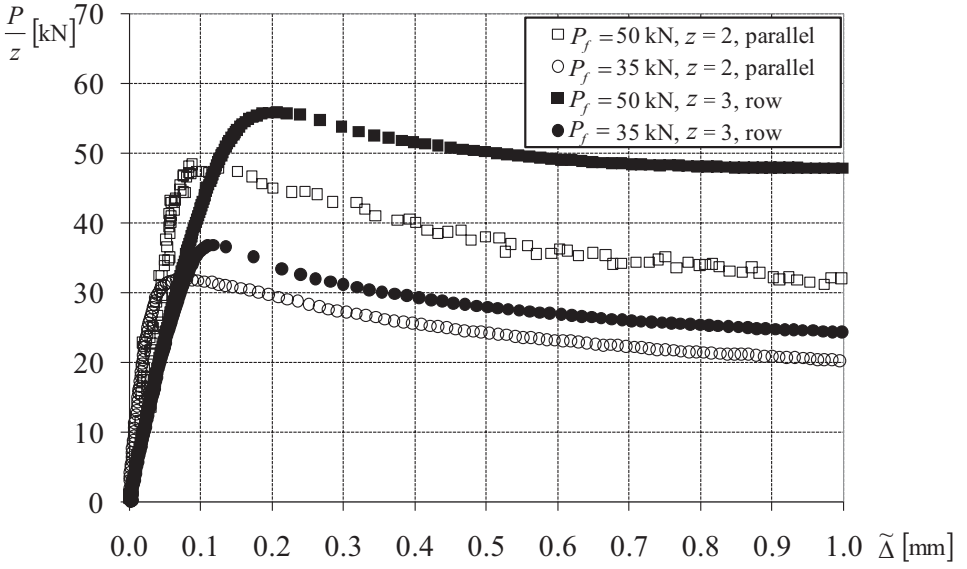

Figure 31. Measured average total response of one fastener for the non-bonded lap-connection interfaces. For scaling, $z = 3$ for the row layouts and $z = 2$ for the parallel connections, has been used.

6 Geometry optimization of off-center loaded layout

The goal of positioning optimization is to find a multi-fastener pattern, which more evenly distribute the resultant shear loads between fasteners, thus reducing the maximum stress in the vicinity of any single fastener. A computationally efficient optimization procedure which makes use of analytical fastener load determination based on the vector sum method (Reilly 1870) is presented. The presented formulation is programmed based on the constrained geometric optimization (The MathWorks 2011b). The equations of the classical vector superposition analysis are derived in a vector calculus form. The representation is particularly suitable for mathematical programming and computing. A typical eccentrically loaded multi-fastener bracket-to-beam joint is studied as an example problem.

6.1 Approximation of shear loads of fastener pattern

The instantaneous centre of rotation (IC) method (Gullander 1914; Kulak et al. 1987; Salmon and Johnson 1996) and the vector superposition method (Reilly 1870; Prichard 1895; Kuzmanović and Willems 1977; Salmon and Johnson 1996) are perhaps the most common analytical assessment methods for determining the slip-critical load of eccentrically loaded multi-fastener joints. Maximum slip resistance of a single fastener is dependent on the fastener pre-tension, the number of slip planes in the fastener system and the slip coefficient. For the IC method, the direction and magnitude of the shear force on a single fastener are dependent on the position of the fastener with respect to the instantaneous centre, IC. By contrast, the vector superposition method assumes that moment in the joint is transferred by all fasteners acting around the centroid of the pattern. Vector superposition and the IC concept of a joint subject to eccentric loading can be illustrated with the help of Figure 32.

6.1.1 Instantaneous centre

For many design situations it is assumed that the eccentric load causes both rotation and translation of the joint. Mechanically this is equivalent to pure rotation about a single point, the instantaneous centre. With reference to Figure 32, the moment on the connection due to joint eccentricity becomes $(\boldsymbol{r}_a - \boldsymbol{r}_b)\times \boldsymbol{p}$ where $\boldsymbol{r}_b$ is the position of IC with respect to centroid c.g. The position of each fastener with respect to c.g. is given by the vector $\boldsymbol{x}^i$ defined by the orthogonal unit vectors $\boldsymbol{e}_1$ and $\boldsymbol{e}_2$ of the coordinate axes x_1 and x_2. The position of the *i*th fastener with respect to IC is defined as $\boldsymbol{r}_c^i$. Therefore, $(\boldsymbol{x}^i - \boldsymbol{r}_b)\times \boldsymbol{p} = \boldsymbol{r}_c^i$. The equilibrium of the system of z fasteners leads to Eqs. (30) and (31) where $\boldsymbol{q}^i$ is the total shear load vector for the fastener *i*.

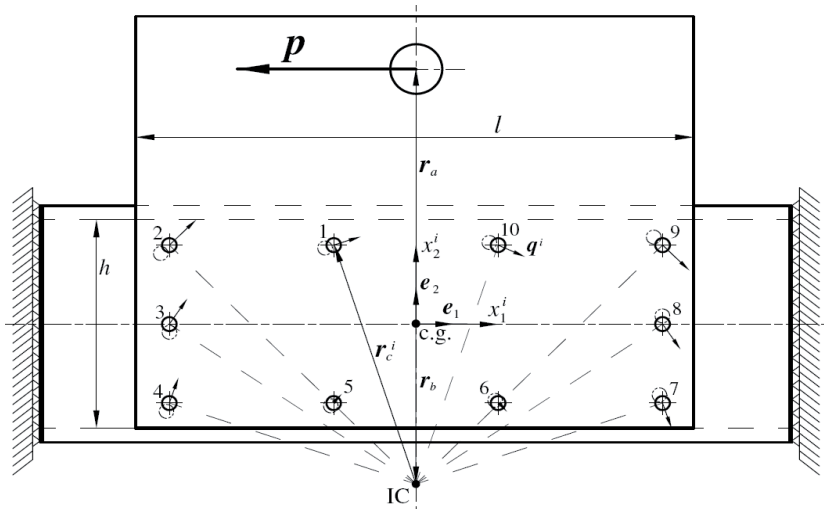

Figure 32. Initial fastener configuration of an eccentrically loaded multi-fastener joint, which is subject to optimization. Each total shear load vector $\boldsymbol{q}^i$ satisfies both the IC and vector superposition concepts in the linear-elastic state.

$$(\boldsymbol{r}_a - \boldsymbol{r}_b)\times \boldsymbol{p} + \sum_{i=1}^{z} \boldsymbol{r}_c^i \times \boldsymbol{q}^i = 0 \tag{30}$$

$$\boldsymbol{p} + \sum_{i=1}^{z} \boldsymbol{q}^i = 0 \tag{31}$$

In the ultimate load case, $\|\boldsymbol{q}^i\|$ is constant valued and is frequently assumed to be equivalent to the computed slip load for a fastener. However, if fatigue is a major design consideration, slip is not desirable. The fastener system should remain fully elastic and $\|\boldsymbol{q}^i\|$ proportional to $\|\boldsymbol{r}_c^i\|$. The position vector of IC, $\boldsymbol{r}_b$ for a fastener pattern is computed by solving Eqs. (30) and (31).

6.1.2 Vector superposition

The elastic vector superposition method assumes that the total shear force for a fastener is the vector sum of two components. The first component is obtained by equally dividing the reaction to the applied direct shear load $\boldsymbol{p}$ on the joint between all fasteners in the pattern. This is expressed in Eq. (32), where $\boldsymbol{q}_p^i$ is the direct shear force vector for the fastener *i* and is assumed to be identical for all fasteners in the pattern.

$$\boldsymbol{q}_p^i = -\boldsymbol{p}/z \tag{32}$$

The second shear force component for a fastener is due to the moment caused by the eccentricity of the joint with respect to c.g. of the fastener pattern,

$$\boldsymbol{m} = \boldsymbol{r}_a \times \boldsymbol{p}. \tag{33}$$

The moment-reaction component for the fastener *i* is given by $\boldsymbol{m}^i = \boldsymbol{x}^i \times \boldsymbol{q}_m^i$. If the basic assumption is made that $\boldsymbol{q}_m^i$ is proportional to the distance of the fastener from c.g., i.e. $\|\boldsymbol{x}^i\|$, the normalized moment contribution is constant for all fasteners,

$$\frac{\boldsymbol{x}^i \times \boldsymbol{q}_m^i}{\|\boldsymbol{x}^i\|^2} = \frac{\boldsymbol{x}^z \times \boldsymbol{q}_m^z}{\|\boldsymbol{x}^z\|^2}, \quad i = 1, 2, \ldots, (z\text{-}1). \tag{34}$$

The total reaction moment from all fasteners in the system is then,

$$\boldsymbol{m}_r = \frac{\boldsymbol{x}^i \times \boldsymbol{q}_m^i}{\|\boldsymbol{x}^i\|^2} \sum_{j=1}^{z} \|\boldsymbol{x}^j\|^2 . \tag{35}$$

For equilibrium, Eqs. (33) and (35) can be equated

$$\boldsymbol{r}_a \times \boldsymbol{p} = \frac{\boldsymbol{x}^i \times \boldsymbol{q}_m^i}{\left\|\boldsymbol{x}^i\right\|^2} \sum_{j=1}^{z} \left\|\boldsymbol{x}^j\right\|^2 . \tag{36}$$

Rearranging Eq. (36) leads to

$$\frac{\boldsymbol{x}^i \times \boldsymbol{q}_m^i}{\left\|\boldsymbol{x}^i\right\|^2} = \frac{\boldsymbol{r}_a \times \boldsymbol{p}}{\sum_{j=1}^{z} \left\|\boldsymbol{x}^j\right\|^2} \tag{37}$$

and because the solution of $\boldsymbol{q}_m^i$ in an implicit form can be written,

$$\boldsymbol{q}_m^i = \frac{\left(\boldsymbol{x}^i \times \boldsymbol{q}_m^i\right) \times \boldsymbol{x}^i}{\left\|\boldsymbol{x}^i\right\|^2} , \tag{38}$$

the moment-reaction shear force vector of the *i*th fastener due to the applied moment is found by substitution of Eq. (37) into Eq. (38)

$$\boldsymbol{q}_m^i = \frac{\left(\boldsymbol{r}_a \times \boldsymbol{p}\right) \times \boldsymbol{x}^i}{\sum_{j=1}^{z} \left\|\boldsymbol{x}^j\right\|^2} . \tag{39}$$

The total shear force for the fastener *i* is the vector sum of the results from Eqs. (32) and (39),

$$\boldsymbol{q}^i = \boldsymbol{q}_m^i + \boldsymbol{q}_p^i . \tag{40}$$

6.2 Layout optimization of the bracket-beam test problem

In this section, a computationally efficient geometric fastener layout optimization problem is formulated. An eccentrically loaded multi-fastener bracket-to-beam connection was evaluated as an example structure subject to optimization. An arc-shaped fastener pattern is presented as an exactly equally stressed configuration based

on the classical vector superposition analysis of eccentrically loaded multi-fastener joints (Reilly 1870).

6.2.1 Optimization problem formulation

Optimization of the eccentrically loaded joint was based on the vector sum method using the initial fastener configuration shown in Figure 32. In this example the number of fasteners is constant, $z = 10$. The objective function Q_f to be minimized was the sum of the magnitudes of shear force on all fasteners in the configuration.

Initial dimensional constraints are applied to determine an allowable design domain D for the fastener group, which is slightly smaller than the l x h overlap region between the bracket and stiffened plate as shown in Figure 33. In this example $l = 2.5h$, and the edge distance between the limits of D and the plate edge was $h/8$. The design variables used in the optimization are each fastener's position vector $\boldsymbol{x}^i$ with respect to c.g. of the pattern.

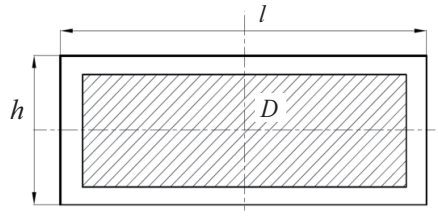

Figure 33. Design domain D for the studied design examples. The area of D is smaller than l x h overlap region due to initial design constraints.

The function *fmincon* included in the MATLAB optimization toolbox (The MathWorks 2011b) was used for the constrained non-linear optimization to find the minimum of Q_f starting from the initial position vectors. The *fmincon* function is based on sequential quadratic programming (SQP), where a quadratic programming sub-problem is solved at every iteration step. Typical to gradient methods, direction search within the design domain and step-size selection are performed. For each iteration step, an estimate of the Hessian of the Lagrangian is updated and a line search is performed using a merit function (The MathWorks 2011b). The SQP method has many advantages; gradients of

only the active constraints are needed, equality constraints can be applied in addition to the inequalities, and the starting vector can significantly differ from the solution (Belegundu and Chandrupatla 2011).

The value of the objective function used in the multi-fastener pattern optimization, i.e. the total shear magnitude sum Q_f, is minimized subject to the condition that an equal shear load magnitude exists at each fastener and a minimum allowable spacing s between the fasteners is maintained. The geometric optimization problem formulation is then (Oinonen et al. 2010):

Min.

$$Q_f = \sum_{i=1}^{z} \left\| \boldsymbol{q}^i \right\| \tag{41}$$

s.t.

$$\left\| \boldsymbol{q}^z \right\| = \left\| \boldsymbol{q}^i \right\|, \; i = 1, 2, \ldots, (z\text{-}1) \tag{42}$$

and

$$s \leq \left\| \boldsymbol{x}^i - \boldsymbol{x}^j \right\|, \; i = 1, 2, \ldots, (z\text{-}1); \; j = (i\text{+}1), \ldots, z. \tag{43}$$

The objective function (41) and constraint equations (42) and (43) are all real valued, continuous and have continuous first derivatives. Constraint Eq. (42) specifies the uniform shear load magnitude on each fastener while constraint Eq. (43) defines an allowable pitch value s, i.e. the minimum distance between any two fasteners is constrained. Constraint Eqs. (42) and (43) determine a maximum value of s with respect to convergence within D.

The following design examples were solved with the largest possible values of s, to maximize an exploitation of D in the vertical direction. A total release of constraint Eq. (43) results to a layout where all fasteners are overlapping at the upper left and right corners of D, because the effect of moment is there reduced to its minimum. In contrast,

the effect of uniform direct shear components $\boldsymbol{q}_p^i$ is not dependent on fastener's positions. The reader with some further interest in possible constraint variations is encouraged to program the represented pattern optimization problem.

6.2.2 Resulted arc-shaped pattern

The computed optimal multi-fastener group based on an assumed uniform direct shear load distribution is presented in Figure 34. In this example, the lower bound for the pitch constraint, i.e. Eq. (43), is $s = 0.251h$. Figure 35 presents the values of one design variable $\boldsymbol{x}^9$ and the value of the objective function Q_f during several iterations of the geometry optimization. The objective function and all design variables were nearly constant after the 7th iteration.

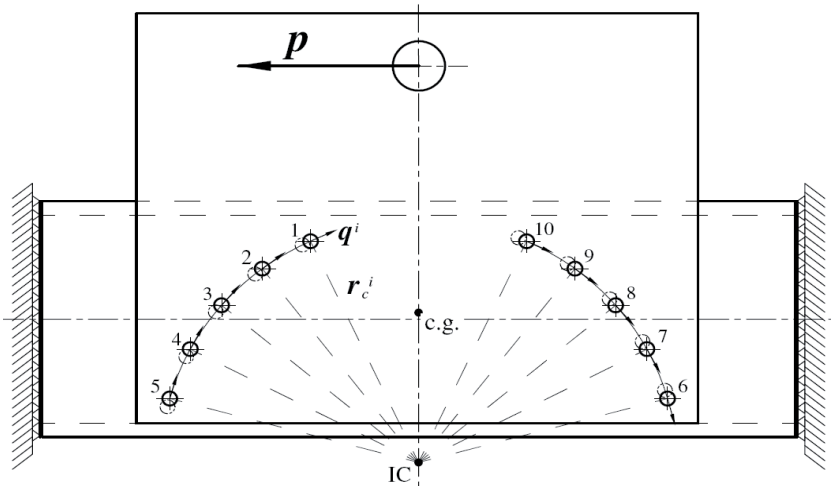

Figure 34. Optimized multi-fastener group with equal direct shear load distribution. The joint, having all fasteners symmetrically distributed about a point loading, is assumed to rotate about the common IC point (Oinonen et al. 2010).

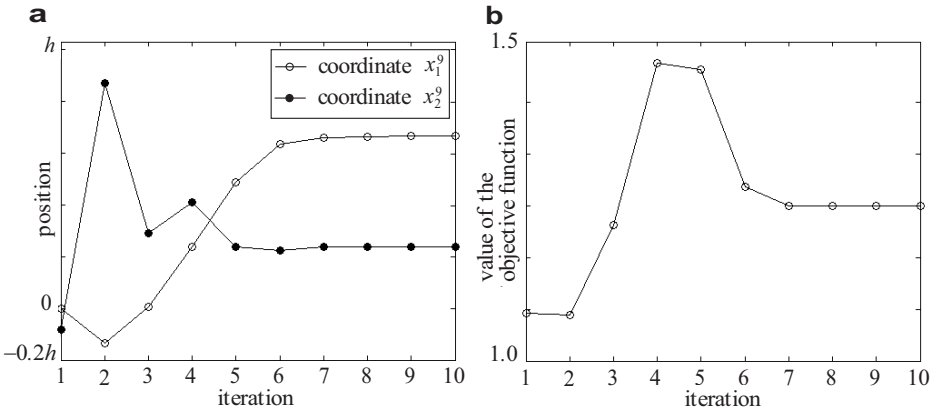

Figure 35. a) Position of the fastener i = 9 in terms of the horizontal and vertical coordinates, x_1^9 and x_2^9. b) Corresponding development of the objective function (normalized value). This converged state corresponds to the pattern shown in Figure 34.

7 Discussion

In the following sections, observations based on the experimental and computational results are provided. Discussion of the interface tests, interface fracture toughness and cohesive zone model is given in Section 7.1. Section 7.2 presents issues related to the testing and modelling of the full-scale double lap-joints and Section 7.3 discusses several issues related to fastener pattern optimisation to reduce local shear stress concentrations. Some suggestions for the related future work are discussed in Section 7.4.

7.1 Adhesive reinforced interfaces

Good accuracy was maintained in manufacturing, preparation and assembly of the napkin ring specimens introduced in Section 2. A tailor made testing device shown in Figure 4 was used for the quasi-static testing procedure. In addition, a very sensitive eddy current sensor with a high resolution was used in the measurements of the relative displacement between the identical specimen halves. See Appendix A for more figures.

The constant B in Eq. (1) represents the contribution of the adhesive reinforcing to the shear strength of the interface τ_{II}^{p}. For a specific surface condition, this value was nearly independent of q. With reference to Table 4, the highest value $B \approx 57$ MPa was obtained for the reinforced fine ground specimens involving 65±3 °C heat cure. For the heat-cured coarse ground and grit blasted interfaces, the respective values were 45.4 and 44.6 MPa. However, for the fine ground and grit blasted interfaces cured at room temperature, the resulted values 40.7 and 17.2 MPa were considerably lower as compared to the corresponding values of B obtained with heat cure. The slope constant A in Eq. (1) determines the rate of increase in interface shear strength with the normal pressure q. Hence, $A \approx \mu_p$, i.e. the dimensionless constant A is approximately equal to the static friction coefficient of the interface. From Table 4, the greatest A can be found for the grit blasted surface finish. With reference to Figure 7, the highest τ_{II}^{p} was obtained for the reinforced grit blasted surface finish for the case q = 150 MPa. It can

also be seen from Figure 7 that the rate of increase of τ_{II}^{p} with q was nearly constant for a particular surface finish for both bonded and non-bonded interfaces. This observation represents the superposition of adhesive strength with interface friction and corresponds to the previously published results obtained using a strong anaerobic adhesive and ground specimen interfaces (Dragoni and Mauri 2000). Moreover, Figure 7 shows that the rate of $\tau_{II}^{p}(q)$ was not sensitive to the curing temperature, i.e. 65±3 or 20±1 °C.

For all interfaces subject to small normal stress, i.e. q = 4 MPa, the shear fracture was fully brittle. Based on Figures 5a-b, the interfacial fracture was due to adhesive failure for both the fine and coarse ground interfaces. In contrast, the grit blasted interface showed predominantly cohesive failure as can be seen from Figure 5c. Due to the differing failure mode for low q as compared to the cases involving the greater normal pre-stress, i.e. $q \in [50,200]$, the data for q = 4 reported in Table 5 was excluded from Figure 7 and from the regression analysis used to calculate A and B. In consequence, the contribution of the reinforcing on the interface in terms of the constants B reported in Table 4 cannot directly be adapted or validated based on the values of τ_{II}^{p} from Table 5. In addition, the values of B listed in Table 4 considerably differ from the shear limits reported by the adhesive manufacturer in Table 2. With reference to Figures 6a-c which were tested with q = 100, predominantly cohesive failure can be observed for all the studied interface types. A comparison of Figures 5c and 6c for grit blasted surfaces shows that low q resulted in a cohesive failure without noticeable damage to the HSS adherents. In contrast for more significant q, the surface is noticeably damaged. The transition from adhesive and brittle failures at low q to predominantly cohesive and ductile or semi-ductile failure at higher q has not been studied in detail and is left for future work.

In the current study, the principle of superposition accurately describes the behaviour of fine ground and grit blasted surfaces, but the fit is less satisfactory for coarse ground surfaces. Figure 9 shows the initial interface degradation response of the coarse ground specimens for the cases q = 150 and q = 200 MPa. Due to the small average increase in τ_{II}^{c} for q = 200 as compared to q = 150, the slope A for the reinforced coarse ground case differs significantly from the non-reinforced case. If the results for q = 200 are excluded, the slope A = 0.19 is calculated, which is more consistent with the observations from other surface finishes. For the coarse ground cases, the relatively

small increase in τ_{II}^{c} between q = 200 and q = 150 resulted, presumably, due to the subsequent unstable decohesion responses. Similar unstable fracture response was observed for the heat-cured grit blasted specimens at q = 200, and these are not discussed as part of this study. The polished micro-sections in Figure 3 show that as surface roughness increases, the contact points between interfaces become more distinct and point-like. When the mode II load is applied under q, it can be expected that local multiaxial yielding occurs causing the interface to collapse. However, a more precise explanation for unstable decohesion propagation of the rougher bonded HSS interfaces involving the high pre-stress, $q \in [150,200]$ has not yet been found.

Data for the adhesive reinforced interfaces shown in Figures 8, 10 and 11 indicates that as $\Delta \to 1.0$ mm, $\tau_{II}(\Delta)$ for all specimens had reached a nearly steady state value. Therefore, the reinforced frictional interfaces can be assumed as fully damaged for $\Delta \geq$ 1.0 mm. The critical interface traction stress t_{II}^{c} and stiffness parameter κ_{II} can be estimated from Figures 10 and 11 for CZM of grit blasted interfaces. With this information, the CZM shown in Figure 17 could be fully defined by applying the non-linear least squares method.

The individual data points in Figures 8-11 were collected at fixed time intervals. Thus, large gaps between points indicate a very rapid increase in relative displacement at the interface. Such gaps are interpreted as representing unstable semi-brittle decohesion. A comparison of Figures 8 and 9 shows more ductility for the coarse ground surface finish when compared to the fine ground in otherwise identical testing conditions. From Figure 9, for Δ > 0.1 mm, unstable decohesion propagation occurred especially for the tests with the highest q. As with the fine ground cases, the brittle fracture occurred for the coarse ground specimens for both q = 50 and q = 100 MPa. From Figure 8 it can be observed, however, that the fine ground interfaces become increasingly ductile as $q \to 200$. This indicates an increasing strength contribution from friction relative to the shear strength of the adhesive. From Figure 10, unstable decohesion response due to the semi-brittle interface fracture is observed. This is seen especially for q = 150 over the range of $\Delta \in (0.1,0.35)$, where there is a sudden decrease in τ_{II} accompanied by an increase in Δ.

The measured $\tau_{II}(\Delta)$ response of the reinforced grit blasted specimens cured at room temperature is shown in Figure 11. The repeated identical tests show excellent

repeatability for q = 100 MPa. Concerning the more conservative results for q = 150 and q = 200, more non-linear initial degradation can be observed as compared to the corresponding results with the higher τ_{II}^{p}. This can be assumed to occur due to the sensitivity to statistical effects of the grit blasting quality and interface's setup process during application of q. In Figure 11, there exists only very small scatter in the response as $\Delta \rightarrow 1.0$ mm, i.e. as the assumed fully damaged state is approached. A comparison of Figures 10 and 11 clearly shows more ductility for the reinforced interfaces cured at room temperature as compared to the similar heat-cured specimens involving identical testing conditions.

Although test data includes moderate statistical scatter, the developed damage evolution model can be assumed to provide realistic results when used in the FEM environment. This claim is supported by the results shown in Figure 19, from where a coherent match between the experimental and simulation results can be observed for the each case of q. With the observed overall scatter in mind, a sensitivity to unification of the material constants can be interpreted as insignificant based on Figures 14 and 19.

Based on Figures 20-22, G_{II}^{c} was attained as $\Delta \rightarrow 1.0$ mm and increased with the higher values of q. A good agreement between the directly numerically integrated experimental data and Eq. (26) can be observed from Figure 20 for both the results involving the unified material parameters and with the constants based on the original individual data sets. However, sensitivity to unification of the material constants can be interpreted as moderate based on Figure 20.

The results for the non-reinforced grit blasted specimens are shown in Figure 15 and for the ground interface finishes in Figure 16. For the grit blasted interfaces, the significant decrease in $\tau_{\mathrm{II}}(1.0)$ involving the decreasing gradient can be noticed especially for the experiment with the highest q. In addition, slip hardening occurred for the non-reinforced coarse ground contact surfaces for all q; this observation corresponds to the previous results by Courtney-Pratt and Eisner (1957). Finally, the experiments on the non-reinforced specimens with the fine ground surface finish most closely followed the classical Coulomb's law of friction.

7.2 Full-scale lap-connections

Determination of the outer limit radius of the annular interface r_a was based on the reference FE model. With reference to Figure 25a, it is observed that the plates deform so as to leave a rather well defined contact surfaces. This contact area for the pre-defined clamping load P_f determines r_a. The normalized normal pressure at the interface computed using the FE model is shown in Figure 27 with comparison to the classical approximation (Rötscher 1927) and more complex analytical solution (Chandrashekhara and Muthanna 1979). These alternative methods to determine r_a were provided in order to present the more direct solutions for a design of reinforced joints, e.g. if no further FEA is considered. The resulted normal pressure $\sigma_3(r)$ distribution calculated using the solution derived by Chandrashekhara and Muthanna (1979) was close to FEA.

The shear fracture was fully brittle for all the experimented adhesive reinforced connection interfaces involving $P_f \in [35,50]$ kN. The grit blasted annular interfaces showed predominantly cohesive fracture as indicated by Figure 24a. See also Appendix B for more details concerning observations on interfacial damage behaviour. For all reinforced specimens listed in Table 8, a sudden fully brittle fracture occurred after attaining the maximum shear load carrying capacity P_p. Two replicate experiments were performed for the reinforced specimens. Attempts to fully determine interfacial degradation behaviour were unsuccessful due to the sudden drop in shear load at P_p.

Using the grit blasted napkin ring specimens with heat cure, the pre-stress independent portion of the interfacial shear stress B was experimentally determined for the normal stress range of $q \in [50,150]$ MPa. Based on Figure 26, $|\sigma_3|(r_b) \approx 150$ MPa, and $q \in [50,150]$ MPa thus involves the normal stress distribution range of the annular connection interface clamped to $P_f = 50$ kN. For $P_f = 35$ kN, $|\sigma_3|(r_b) \approx 110$ MPa. These observations were assumed to justify the use of $B = t_{\mathrm{II}}^c$, i.e. the critical interface traction stress of the CZM shown in Figure 17a. With reference to Figure 26, the solution of $r_a \approx 19$ mm was obtained from the abscissa as the normal stress at the interface $\sigma_3(r) \to 0$. For both the test specimens and damage simulations, the outer limit radius of the annular interface was selected to $r_a = 20$. This small rounding was done due to assumed over closure of rough contact surfaces subject to P_f. Interfacial micro-

slipping was not allowed, and therefore the interface stiffness parameter was selected to $\kappa_{II} = \infty$. With these definitions, simulations closely resembled to the experimental observations on the full-scale test specimens. Based on the fundamental experimental data presented in Figures 10 and 11, $\kappa_{II} \in [3 \cdot 10^3, 10^4]$ N/mm^3 can be approximated. The use of $\kappa_{II} \in [3 \cdot 10^3, 10^4]$ in trial simulations, however, did not improve the linear-elastic slopes of computed $P(\tilde{\Delta})$ as compared to the corresponding measured responses.

With reference to Figures 29 and 30, P_p of the adhesive reinforced lap-joints is not sensitive to the pre-load of the bolts for the range $P_f \in [35,50]$ kN. Hence, the contribution of the reinforcement bonding on P_p is significant. A good agreement between the test and simulation results was observed until attaining P_p. However, the exceptions were the replicate experiments on the parallel lap-connections involving P_f = 35 kN. This diverging result can be explained with the help of Figure 25b. Opening of the interface can be observed on the right side due to the combined loads P_f and P. In consequence, the corresponding left half is closing due to elastic continuum behaviour. This non-linear effect most influences on the first fastener of the row joint, i.e. the bolt nearest to P. Therefore, single fastener connections are more influenced on this phenomenon than multi-fastener row connections. When the number of fasteners z in a row connection is increased, the computed P_p / z decreases as can be observed from Table 9. This occurs due to elastic continuum behaviour.

The simulated $P(\tilde{\Delta})$ responses have exclusively been validated until $\tilde{\Delta}$ corresponding to P_p due to the experimentally observed sudden brittle fracture of the connection interfaces. Despite the previous fact, an assumed softening part was included in the adapted CZM shown in Figure 17a and simulation runs were computed until the full damage was accumulated. Consistently, Figures 29 and 30 show that the computed $P(\tilde{\Delta})$ are approaching to the steady state involving exclusively frictional behaviour as $\tilde{\Delta} \to 1.0$ mm.

Based on Figure 31, $P(\tilde{\Delta})$ of the non-bonded lap-joints involving $P_f \in [35,50]$ follow expected degradation behaviour, i.e. wear of HSS. In contrast to the reinforced interfaces, P_p of the identical non-bonded connections can be observed as sensitive to P_f. This is the disadvantage of non-bonded lap-joints also due to the known challenges in tightening of HS bolts to the precise P_f (Kulak et al. 1987; Bouwman and Piraprez 1989). The measured responses of the non-bonded test specimens presented in Figure

31 show that P_p / z was clearly higher for the row connections as compared to the parallel layout with $P_f \in [35,50]$ kN. With reference to Figure 25b, this presumably occurred due to concentration of σ_3 at the left portion of the interface. Consequently, the local high σ_3 plastically deformed the rough contact surfaces resulting to highly damaged HSS. To this end, recall the fundamental data based on the non-bonded napkin ring specimens presented in Figure 15.

7.3 Positioning optimization of fasteners

For eccentrically loaded multi-fastener joints, the traditional elastic vector sum concept, which assumes that the direct shear load is evenly divided among all fasteners, is computationally convenient. In the current study, geometric optimization was based on the vector superposition method using the traditional uniform direct shear load assumption. The use of the function *fmincon* included in the MATLAB optimization toolbox (The MathWorks 2011b) which exploits SQP was effective for the cases in this study due to the number of variables in which both the objective function and constraints were non-linear functions of the design variables.

As can be seen from Figure 34, the assumed direct shear load distribution has led to an arc-shaped fastener distribution. The arc radius depends on the spacing constraint *s* and the eccentricity of the joint loading $\boldsymbol{r}_a$. The connection, having all fasteners symmetrically distributed about an eccentric point load, was assumed to rotate about the common IC point (Gullander 1914). In order to justify this assumption, both the bracket and boom plates have to follow linear-elastic behaviour (Muir and Thornton 2004; Oinonen et al. 2010).

With reference to Figure 35, ten iteration runs were needed to obtain final convergence. Figure 35b shows that the initial objective function value was lower than the final converged value. In this case, however, the constraint equations were not initially satisfied. The initial coordinate estimates for the fasteners were far from the final optimized values, indicating the robustness of the mathematical optimization tool used.

7.4 Future research

The main limitation in the modelling of full-scale adhesive reinforced bolted lap-connections is due to an assumption that interfacial damage does not depend on variation of the normal stress during application of the direct shear load. Shear lag in the joint necessarily causes the normal pressure to change during tensile loading. The assumption of a constant normal pressure can lead to non-conservative estimates in the case of interfaces which are sensitive to releasing of the normal pre-stress. The dependency between the normal pre-stress and material model could be incorporated in FEM using the solution dependent state variables (ABAQUS Inc 2010). However, the aspect of variation of the mode I stress during the direct mode II loading still lacks experimental validation. Therefore, the FEM implementation of the more complex CZM with contact pressure monitoring is left for future work. In addition, an extensive experimental programme would be needed to be initiated.

The current study has been limited to include only the linear elastic strength of HSS plate members. This assumption is justified due to the very high yield strength of the HSS plates. If applicable, e.g. von Mises plasticity could be included in ABAQUS/Explicit based FEA. Moreover, the current thesis is exclusively concentrated with the quasi-static assessment of adhesive reinforced frictional connections. Fatigue and cyclic slip behaviour of the identical reinforced specimens are currently being studied as an alternative joining method for thin sheet structures in HSS (Hurme et al. 2011).

8 Conclusions

In this thesis, new fundamental information on combined decohesive and frictional behaviour of epoxy reinforced interfaces has been developed and adapted to computational mechanics using cohesive zone model (CZM) and non-local friction laws.

The influence of the clamping load, surface roughness and cure temperature of epoxy on the quasi-static shear strength of mechanically clamped high strength steel (HSS) interfaces reinforced with adhesive have been studied experimentally. Interface constants for the computational damage evolution model have been fitted based on the least squares method. The shear energy release rate vs. relative displacement curves have been plotted. A shear damage evolution modelling procedure that can be incorporated in the finite element method (FEM) has been suggested. The FEM based damage modelling procedure developed for 2D has been applied to the interface damage simulations on the full-scale adhesive reinforced bolted double lap-joints.

A computationally efficient fastener layout optimization problem has been formulated and programmed based on constrained geometric optimization. The equations of the classical vector superposition analysis have been derived in a vector calculus form. An eccentrically shear loaded multi-fastener bracket-to-beam connection has been studied as the example problem.

The following conclusions can be summarized based on the main results reported and discussed in this thesis.

1. For each of the three surface finishes tested, the shear strength of the bonded and non-bonded interfaces increased at a near constant rate with normal pressure. Therefore, for abraded HSS interfaces reinforced with high modulus epoxy, the principle of superposition is applicable.
2. The contribution of the epoxy adhesive to the total shear strength of the interface varied with interface roughness. It was found to be highest for the fine ground surface finish and lowest for the grit blasted surfaces.

3. For all values of normal pressure, the epoxy reinforced grit blasted interfaces with heat cure resulted in the highest measured total shear stress values τ_{II}^{p}. Hence, both surface roughness and cure temperature significantly influence on the quasi-static shear load carrying capacity of adhesive reinforced interfaces.
4. The maximum observed residual slip-strength after full decohesion, i.e. as the relative interface displacement approached 1.0 mm, was found to be considerably higher for the grit blasted reinforced interfaces as compared to the corresponding non-bonded cases.
5. For 1.0 mm relative interface displacement, the highest value of the critical fracture energy release rate G_{II}^{c} was attained for the heat-cured grit blasted interfaces. The value of G_{II}^{c} increased with normal pressure for all surface finishes. This was due to the increased work needed to locally deform the contacting HSS surfaces.
6. The epoxy reinforced grit blasted connection interfaces with heat cure can be considered suitable for engineering applications. Joint strength was good in comparison to other studied interface combinations and the failure mode was partially ductile.
7. Based on the 2D test problem, the computed FE solution of the total shear stress vs. relative displacement response $\tau_{II}(\Delta)$ showed a very good correlation with the corresponding experimental data points.
8. Data from the small-scale specimens could be adequately adapted to full-scale joints using the developed CZM and non-local friction. When implemented in FEA, the computed ultimate shear load capacity of the full-scale double lap-joints were in good agreement with experimentally measured values. Hence, the presented modelling procedure can be suggested to be used for engineering of adhesive reinforced connection interfaces involving friction.
9. The contribution of the adhesive reinforcement to the ultimate shear load capacity of the full-scale lap-joint specimens was significant. Fastener pre-load had significant influence on the shear load capacity of the non-bonded full-scale lap-joints but had less influence on the capacity of adhesive reinforced interfaces.

10. The computed ultimate shear load capacity corresponding to the contribution of one fastener decreased as the number of fasteners in the row (series) connection was increased.
11. The annular interfacial areas can be considered as local attachment points in large-scale structures. Hence, the modelling procedure presented in this thesis is very attractive when the positioning optimization of adhesive reinforced multi-fastener connection interfaces is considered.
12. As the result of the positioning optimization, an arc-shaped fastener pattern satisfies the exactly equally loaded configuration of fasteners based on the classical vector superposition analysis. More uniform distribution of the fastener loads should help to prevent interfacial shear fracture and slipping of the joint and thus improve the structural strength.

References

ABAQUS Inc (2010) ABAQUS User's manual - Version 6.10-1.

Adams RD, Wake WC (1984) Structural adhesive joints in engineering. Elsevier Applied Science Publishers Ltd, England

Albrecht P, Sahli AH (1986) Fatigue strength of bolted and adhesive bonded structural steel joints. In: Potter JM, ed. Fatigue in mechanically fastened composite and metallic joints (STP 927). ASTM, Philadelphia, pp. 72-94

Albrecht P, Sahli AH (1988) Static strength of bolted and adhesively bonded joints for steel structures. In: Johnson WS, ed. Adhesively bonded joints: Testing, analysis, and design (STP 981). ASTM, Philadelphia, pp. 229-51

Ali M, Lorrain B, Karama M, Puel B (2007) Fatigue behaviour of the screwed/riveted joints and the bonded joints. Fatigue Des 2007: W1.6 - Methodologies and tools for fatigue life assessment for assemblies, Senlis

Allix O, Ladevéze P, Corigliano A (1995) Damage analysis of interlaminar fracture specimens. Compos Struct 31:61-74

Archard JF (1953) Contact and rubbing of flat surfaces. J Appl Phys 24:981-8

Archard JF (1957) Elastic deformation and the laws of friction. Proc Roy Soc London (Ser A) Math Phys Sci 243:190-205

ASTM International (2009) ASTM standards on disc: Adhes 15.06

Bao G, Suo Z (1992) Remarks on crack-bridging concepts. Appl Mech Rev 45:355-66

Bathe KJ (1996) Finite element procedures. Prentice-Hall Inc, New Jersey

Belegundu AD, Chandrupatla TR (2011) Optimization concepts and applications in engineering (2nd ed). Cambridge University Press, New York

Belytschko T, Liu WK, Moran B (2001) Nonlinear finite elements for continua and structures. John Wiley & Sons Ltd, Chichester

Birkemoe PC, Srinivasan R (1971) Fatigue of bolted high strength structural steel. J Struct Div 97:935-51

Bouwman LP, Piraprez E (1989) The tightening of high-strength bolts in Europe. Steel Constr Today 3:18-25

Broek D (1984) Elementary engineering fracture mechanics (3rd ed). Kluwer Academic Publishers Group, the Netherlands

Camanho PP, Dávila CG (2002) Mixed-mode decohesion finite elements for the simulation of delamination in composite materials. NASA/TM-2002-211737

Camanho PP, Dávila CG, de Moura MFSF (2003) Numerical simulation of mixed-mode progressive delamination in composite materials. J Compos Mater 37:1415-38

Chan WS, Vedhagiri S (2001) Analysis of composite bonded/bolted joints used in repairing. J Compos Mater 35:1045-61

Chai H (1988) Shear fracture. Int J Fract 37:137-59

Chai H (2004) The effects of bond thickness, rate and temperature on the deformation and fracture of structural adhesives under shear loading. Int J Fract 130:497-515

Chandrashekhara K, Muthanna SK (1979) Analysis of a thick plate with a circular hole resting on a smooth rigid bed and subjected to axisymmetric normal load. Acta Mech 31:33-44

Chickermane H, Gea HC, Yang RJ, Chuang CH (1999) Optimal fastener pattern design considering bearing loads. Struct Optim 17:140-6

Courtney-Pratt JS, Eisner E (1957) The effect of a tangential force on the contact of metallic bodies. Proc Roy Soc London (Ser A) Math Phys Sci 238:529-50

Dávila CG, Camanho PP (2001) Decohesion elements using two and three-parameter mixed-mode criteria. Am Helicopter Soc Conf, Williamsburg 29 October - 1 November

De Bruyne NA (1962) The measurement of the strength of adhesive and cohesive joints. In: Weiss P, ed. Adhesion and cohesion. Proc Symp Adhes Cohes, GM Res Lab, Elsevier Publishing Company, Warren Michigan, pp. 47-64

De Moura MFSF, Chousal JAG (2006) Cohesive and continuum damage models applied to fracture characterization of bonded joints. Int J Mech Sci 48:493-503

De Moura MFSF (2008) Progressive damage modelling. In: Da Silva LFM, Öchsner A, eds. Modeling of adhesively bonded joints. Springer-Verlag, Berlin Heidelberg, pp. 155-82

Doyle G, Pethrick RA (2009) Environmental effects on the ageing of epoxy adhesive joints. Int J Adhes Adhes 29:77-90

Dragoni E, Mauri P (2000) Intrinsic static strength of friction interfaces augmented with anaerobic adhesives. Int J Adhes Adhes 20:315-21

Dragoni E, Mauri P (2002) Cumulative static strength of tightened joints bonded with anaerobic adhesives. Proc Inst Mech Eng (Part L) J Mater - Des Appl 216:9-15

Fays S (2003) Adhesive Bonding Technology in the Automotive Industry. Adhes Interface 4:37-48

Galambos TV, Reinhold TA, Ellingwood B (1982) Serviceability limit states: Connection slip. J Struct Div 108:2668-80

Gould HH, Mikic BB (1972) Areas of contact and pressure distribution in bolted joints. J Eng Indust, August, pp. 864-70

Gough HJ (1924) The fatigue of metals. Scott, Greenwood & Son, London

Gresnigt AM, Stark JWB (1995) Design of bolted connections with injection bolts. In: Bjorhovde R, Colson A, Zandonini R, eds. Connections in steel structures III - behavior, strength and design. Proc Third Int Workshop, Trento, 29 - 31 May, pp. 77-87

Greenwood JA, Williamson JBP (1966) Contact of nominally flat surfaces. Proc Roy Soc London (Ser A) Math Phys Sci 295:300-19

Gullander P (1914) Eccentric rivet connections. Eng Rec 70:518

Hansen NG (1959) Fatigue tests of joints of high strength steels. J Struct Div 85:51-69

Hart-Smith LJ (1985) Bonded-bolted composite joints. J Aircr 22:993-1000

Hobbacher A (2007) Recommendations for fatigue design of welded joints and components. IIW doc XIII-2151-07/XV-1254-07

Hurme S, Oinonen A, Marquis G (2011) Fatigue of bonded steel interfaces under cyclic shear loading and static normal stress. Eng Fract Mech 78:1644-56

Imanaka M, Haraga K, Nishikawa T (1993) Fatigue strength of adhesive/rivet combined joints. Proc Conf Adhes '93, York, UK, 6 - 8 September, pp. 187-92

Kelly G (2005) Load transfer in hybrid (bonded/bolted) composite single-lap joints. Compos Struct 69:35-43

Khrulev VM (1965) Surface roughness and rheological properties of adhesives as factors determining optimal thickness of glue line. Mech Compos Mater 1:61-3

Kim J, Yoon JC, Kang BS (2007) Finite element analysis and modeling of structure with bolted joints. Appl Math Model 31:895-911

Kinloch AJ (1987) Adhesion and adhesives: Science and technology. Chapman & Hall

Krueger R, Cvitkovich MK, O'Brien TK, Minguet PJ (2000) Testing and analysis of composite skin/stringer debonding under multi-axial loading. J Compos Mater 34: 1263-1300

Kulak GL, Fisher JW, Struik JHA (1987) Guide to design criteria for bolted and riveted joints (2nd ed). John Wiley & Sons Inc

Kuzmanović BO, Willems N (1977) Steel design for structural engineers. Prentice-Hall Inc, New Jersey

Love AEH (1944) A treatise on the mathematical theory of elasticity (4th ed). Dover Publications, New York

Mays GC, Hutchinson AR (1992) Adhesives in civil engineering. Cambridge University Press, New York

Mann JY, Pell RA, Jones R, Heller M (1985) Reducing the effects of rivet holes on fatigue life by adhesive bonding. Theor Appl Fract Mech 3:113-24

Matsui K (1990) Effects of curing conditions and test temperatures on the strength of adhesive-bonded joints. Int J Adhes Adhes 10:277-84

Mengel R, Häberle J, Schlimmer M (2007) Mechanical properties of hub/shaft joints adhesively bonded and cured under hydrostatic pressure. Int J Adhes Adhes 27:568-73

Muir LS, Thornton WA (2004) Exploring the true geometry of the inelastic instantaneous center method for eccentrically loaded bolt groups. In: Bijlaard FSK, Gresnigt AM, van der Vegte GJ, eds. Proc 5th Int Workshop Connect Steel Struct V - behaviour, strength & design, Amsterdam, 3 - 4 June, pp. 281-6

Nairn JA (2009) Analytical and numerical modeling of R curves for cracks with bridging zones. Int J Fract 155:167-81

Needleman A (1987) A continuum model for void nucleation by inclusion debonding. J Appl Mech 54:525-31

Oden JT, Martins JAC (1985) Models and computational methods for dynamic friction phenomena. Comput Method Appl Mech Eng 52:527-634

Oinonen A, Marquis G (2009) A procedure for damage modelling of shear loaded structural hybrid interfaces. Proc 10th Finn Mech Day, Jyväskylä, 3 - 4 December, pp. 286-95

Oinonen A, Marquis G (2010) A new shear decohesion damage function for combined clamped and bonded interfaces. 18th Eur Conf Fract, Dresden, 30 August - 3 September

Oinonen A, Marquis G (2011a) A parametric shear damage evolution model for combined clamped and adhesively bonded interfaces. Eng Fract Mech 78:163-74

Oinonen A, Marquis G (2011b) Shear decohesion of clamped abraded steel interfaces reinforced with epoxy adhesive. Int J Adhes Adhes 31:550-8

Oinonen A, Tanskanen P, Björk T, Marquis G (2010) Pattern optimization of eccentrically loaded multi-fastener joints. Struct Multidisc Optim 40:597-609

Paroissien E, Sartor M, Huet J, Lachaud F (2007) Analytical two-dimensional model of a hybrid (bolted/bonded) single-lap joint. J Aircr 44:573-82

Pirondi A, Moroni F (2009) Clinch-bonded and rivet-bonded hybrid joints: Application of damage models for simulation of forming and failure. J Adhes Sci Technol 23:1547-74

Prichard HS (1895) Standard connections for rolled beams. Eng News XXXIII:318-9

Reemsnyder HS (1975) Fatigue life extension of riveted connections. J Struct Div 101:2591-608

Reemsnyder H (1996) Fatigue of mechanically fastened joints. In: ASM Handbook (Vol. 19, Fatigue and Fracture). ASM International, pp. 287-94

Reilly C (1870) Studies of iron girder bridges, recently executed, illustrating some applications of the modern theory of the elastic resistance of materials. Minute Proc Inst Civ Eng XXIX:403-500

Renvall S, Oinonen A, Marquis G (2010) The influence of static normal stress on shear capacity of bonded high strength steel interfaces. 9th Int Conf Multiaxial Fatigue Fract, Parma, 7 - 9 June

Rice JR (1968a) A Path independent integral and the approximate analysis of strain concentration by notches and cracks. J Appl Mech 35:379-86

Rice JR (1968b) Mathematical analysis in the mechanics of fracture. In: Liebowitz H, ed. Fracture: An advanced treatise (Vol. 2, Mathematical fundamentals). Academic Press, New York, pp. 191-311

Richardson RSH, Nolle H (1976) Surface friction under time-dependent loads. Wear 37:87-101

Rutenberg A (1984) Nonlinear analysis of eccentric bolted connections. Eng J 227-36

Rötscher F (1927) Die maschinenelemente (erster band). Verlag von Julius Springer, Berlin

Salmon CG, Johnson JE (1996) Steel structures: Design and behavior (4th ed). Prentice-Hall Inc, New Jersey

Sawa T, Yoneno M, Motegi Y (2001) Stress analysis and strength evaluation of bonded shrink fitted joints subjected to torsional loads. J Adhes Sci Technol 15:23-42

Sellgren U, Björklund S, Andersson S (2003) A finite element-based model of normal contact between rough surfaces. Wear 254:1180-8

SFS-ENV 1993-1-3 Eurocode 3: Design of steel structures (Part 1-3, General rules; Supplementary rules for cold formed thin gauge members and sheeting). Finnish Standards Association, Helsinki

Shahid M, Hashim SA (2002) Effect of surface roughness on the strength of cleavage joints. Int J Adhes Adhes 22:235-44

Stewart I, Chambers A, Gordon T (2007) The cohesive mechanical properties of a toughened epoxy adhesive as a function of cure level. Int J Adhes Adhes 27:277-87

Swift T (1984) Fracture analysis of stiffened structure. In: Chang JB, Rudd JL, eds. Damage tolerance of metallic structures: Analysis methods and applications (STP 842). ASTM, Ann Arbor, pp. 69-107

The MathWorks (2011a) Optimization Toolbox - Least Squares (Curve Fitting). Accessed 27 April. Available via http://www.mathworks.com/help/toolbox/optim/

The MathWorks (2011b) Optimization Toolbox - Constrained Nonlinear Optimization Algorithms - fmincon SQP Algorithm. Accessed 27 April. Available via http://www.mathworks.com/help/toolbox/optim/

Turon A, Dávila CG, Camanho PP, Costa J (2006) An engineering solution for mesh size effects in the simulation of delamination using cohesive zone models. Eng Fract Mech 74:1665-82

Tvergaard V, Hutchinson JW (1996) On the toughness of ductile adhesive joints. J Mech Phys Solid 20:789-800

Uehara K, Sakurai M (2002) Bonding strength of adhesives and surface roughness of joined parts. J Mater Process Technol 127:178-81

Valoroso N, Champaney L (2006) A damage-mechanics-based approach for modelling decohesion in adhesively bonded assemblies. Eng Fract Mech 73:2774-801

Wegman RF (1989) Surface preparation techniques for adhesive bonding. Noyes Publications, New Jersey

Yoshimi I (2008) Modular design for machine tools. The McGraw-Hill Companies Inc, New York

Zhong ZH (1993) Finite element procedures for contact-impact problems. Oxford University Press Inc, New York

3M United Kingdom PLC (2001) Scotch-Weld™ EPX™ Epoxy adhesive DP760 product data sheet

Appendix A - Details of the testing device and specimens

In this Appendix, the supplementary photographs and sketches for Section 2 are provided. The polished micro-sections of the tangential bond line of the contact interfaces shown in Figure 3 were produced using the assembly shown in Figure A5a.

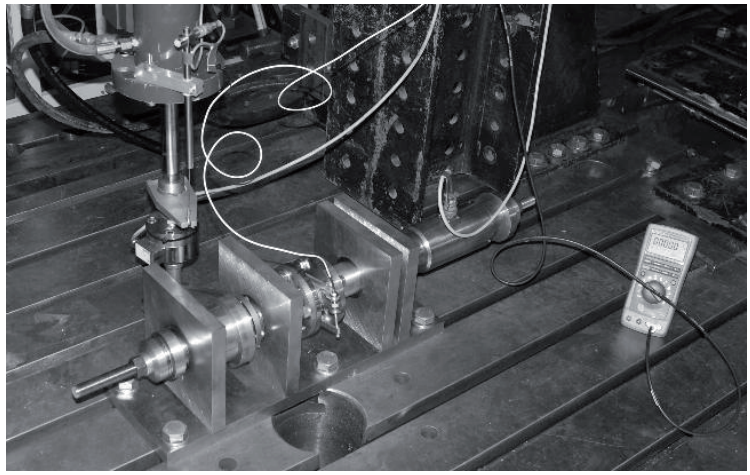

Figure A1. Pure shear loading is applied via the level arm.

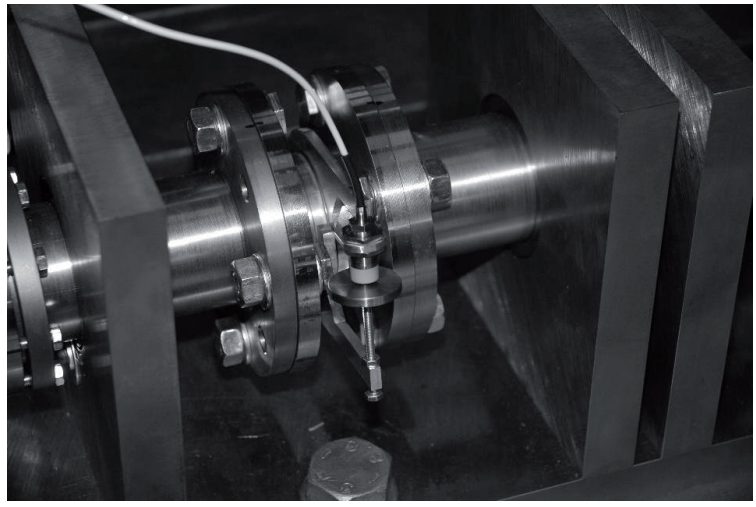

Figure A2. The eddy current sensor and its counterpart are directly attached onto the halves of the napkin ring specimen pair.

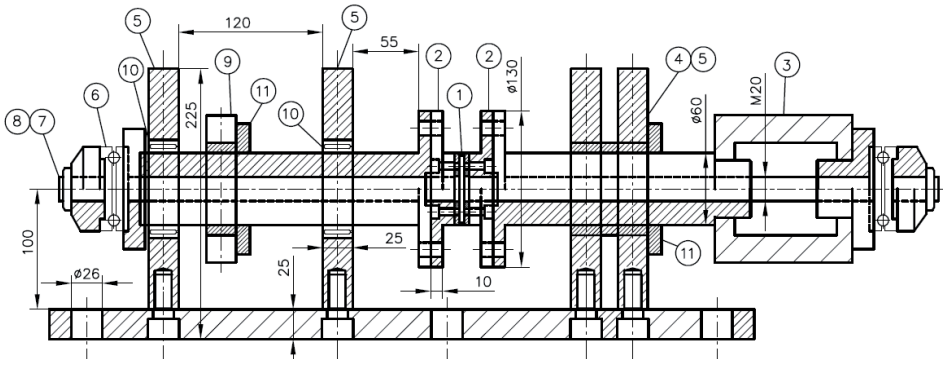

Figure A3. Assembly sketch of the testing device. The key components are: (1) specimen pair, (2) specimen holder, (3) axial load cell, (4) torque reaction, (5) support, (6) thrust bearing, (7) threaded rod, (8) nut, (9) torque arm, (10) rotation bearing, and (11) locking bushing.

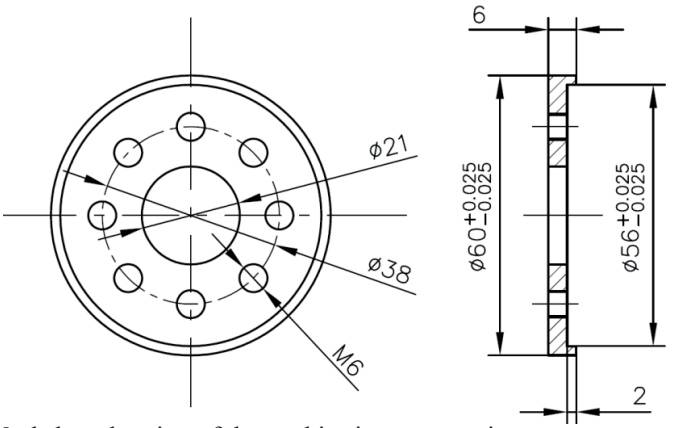

Figure A4. Workshop drawing of the napkin ring test specimen.

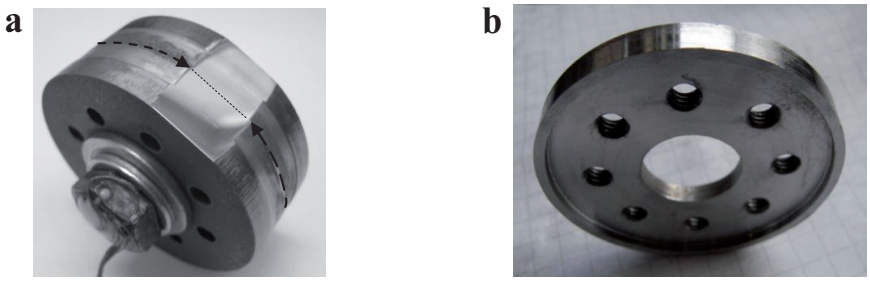

Figure A5. a) The instrumented bolt is used to load the epoxy reinforced specimen interface to the normal pressure q = 100 MPa. The polished interface marked by the dashed curve was examined using a microscope. Two outer disks (similar specimens) are used as the strong washers. b) General photograph of the napkin ring test specimen.

Appendix B - Observations on full-scale adhesive reinforced bolted lap-joints

In this Appendix, some supplementary material for Chapter 5 is provided. With the help of Figure B1, the predominant failure mechanism of the adhesive reinforced bolted lap-connection interfaces can be qualified. Figure B2 illustrates the assembled and instrumented double lap-joint specimen.

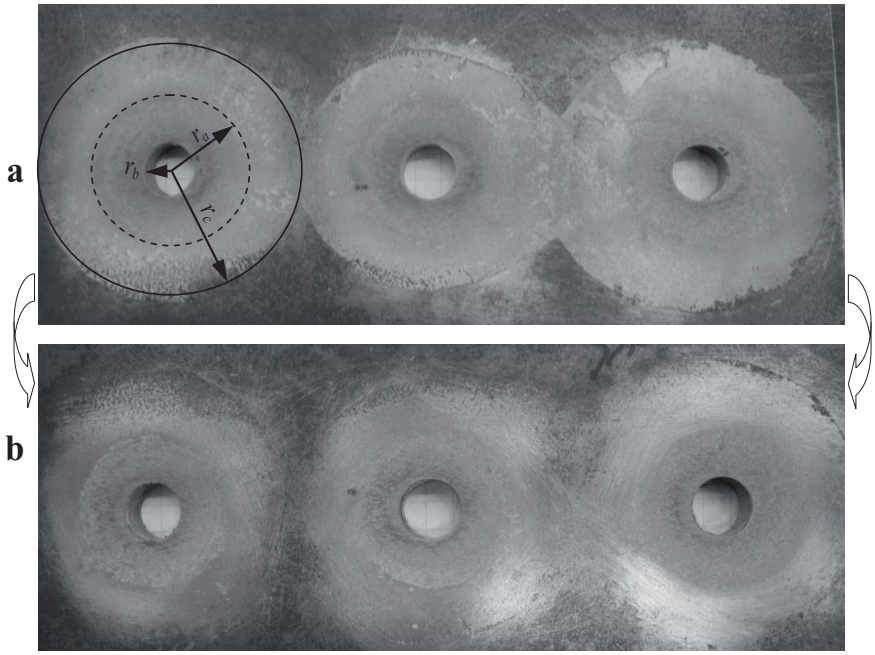

Figure B1. Damaged contact surfaces of the adhesive reinforced multi-fastener lap-connection. Only the case with the clamping load P_f = 35 kN is shown here, but the observation for P_f = 50 kN was similar. Predominantly cohesive damage can be observed for the grit blasted area determined by $r \in (r_b, r_a)$. In contrast for $r \in (r_a, r_c)$, interfacial damage is predominantly adhesive due to the smoother (ground) surface finish. Moreover, for $r > r_a$, the interface opens due to geometric non-linearity, see from Figure 25. The average outer limit radius of the flow of uncured adhesive was measured, $r_c \approx 36 \pm 8$ mm. The photographs a) and b) correspond to the mating surfaces, which were in the contact during shear testing.

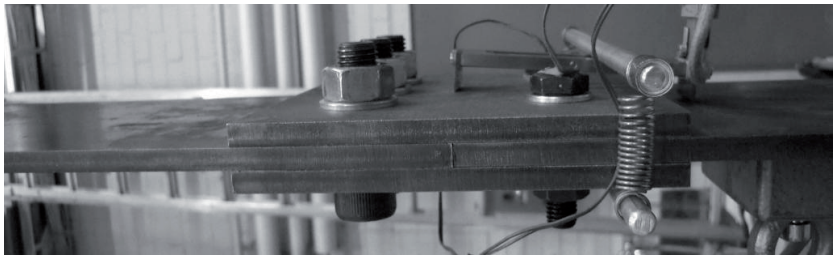

Figure B2. Positioning and attachment of the displacement transducer for the full-scale double lap-joint specimen. See also Figure 23.

Aalto-DD 91/2011

ISBN 978-952-60-4305-0 (pdf)
ISBN 978-952-60-4304-3
ISSN-L 1799-4934
ISSN 1799-4942 (pdf)
ISSN 1799-4934

Aalto University
School of Engineering
Department of Applied Mechanics
www.aalto.fi

BUSINESS + ECONOMY

ART + DESIGN + ARCHITECTURE

SCIENCE + TECHNOLOGY

CROSSOVER

DOCTORAL DISSERTATIONS